

## ACCEPTED VERSION

Cheryl Suwen Law, Yee Lim, Raeanne M. Macalincag, Andrew D. Abell, and Abel Santos  
**Light-confining nanoporous anodic alumina microcavities by apodized stepwise pulse anodization**

ACS Applied Nano Materials, 2018; 1(9):4418-4434

This document is the Accepted Manuscript version of a Published Work that appeared in final form in ACS Applied Materials and Interfaces, copyright © 2018 American Chemical Society after peer review and technical editing by the publisher. To access the final edited and published work see <http://dx.doi.org/10.1021/acsanm.8b00494>

### PERMISSIONS

<http://pubs.acs.org/page/4authors/jpa/index.html>

The new agreement specifically addresses what authors can do with different versions of their manuscript – e.g. use in theses and collections, teaching and training, conference presentations, sharing with colleagues, and posting on websites and repositories. The terms under which these uses can occur are clearly identified to prevent misunderstandings that could jeopardize final publication of a manuscript (**Section II, Permitted Uses by Authors**).

### [Easy Reference User Guide](#)

**7. Posting Accepted and Published Works on Websites and Repositories:** A digital file of the Accepted Work and/or the Published Work may be made publicly available on websites or repositories (e.g. the Author's personal website, preprint servers, university networks or primary employer's institutional websites, third party institutional or subject-based repositories, and conference websites that feature presentations by the Author(s) based on the Accepted and/or the Published Work) under the following conditions:

- It is mandated by the Author(s)' funding agency, primary employer, or, in the case of Author(s) employed in academia, university administration.
- If the mandated public availability of the Accepted Manuscript is sooner than 12 months after online publication of the Published Work, a waiver from the relevant institutional policy should be sought. If a waiver cannot be obtained, the Author(s) may sponsor the immediate availability of the final Published Work through participation in the ACS AuthorChoice program—for information about this program see <http://pubs.acs.org/page/policy/authorchoice/index.html>.
- If the mandated public availability of the Accepted Manuscript is not sooner than 12 months after online publication of the Published Work, the Accepted Manuscript may be posted to the mandated website or repository. The following notice should be included at the time of posting, or the posting amended as appropriate:  
"This document is the Accepted Manuscript version of a Published Work that appeared in final form in [JournalTitle], copyright © American Chemical Society after peer review and technical editing by the publisher. To access the final edited and published work see [insert ACS Articles on Request author-directed link to Published Work, see <http://pubs.acs.org/page/policy/articlesonrequest/index.html>]."  
• The posting must be for non-commercial purposes and not violate the ACS' "Ethical Guidelines to Publication of Chemical Research" (see <http://pubs.acs.org/ethics>).
- Regardless of any mandated public availability date of a digital file of the final Published Work, Author(s) may make this file available only via the ACS AuthorChoice Program. For more information, see <http://pubs.acs.org/page/policy/authorchoice/index.html>.

**18 November 2019**

<http://hdl.handle.net/2440/116316>

## Light-Confining Nanoporous Anodic Alumina Microcavities by Apodized Stepwise Pulse Anodization

Cheryl Suwen Law, Siew Yee Lim, Raeanne Macalincag, Andrew D. Abell, and Abel Santos

*ACS Appl. Nano Mater.*, **Just Accepted Manuscript** • DOI: 10.1021/acsanm.8b00494 • Publication Date (Web): 28 Aug 2018

Downloaded from <http://pubs.acs.org> on August 30, 2018

### Just Accepted

“Just Accepted” manuscripts have been peer-reviewed and accepted for publication. They are posted online prior to technical editing, formatting for publication and author proofing. The American Chemical Society provides “Just Accepted” as a service to the research community to expedite the dissemination of scientific material as soon as possible after acceptance. “Just Accepted” manuscripts appear in full in PDF format accompanied by an HTML abstract. “Just Accepted” manuscripts have been fully peer reviewed, but should not be considered the official version of record. They are citable by the Digital Object Identifier (DOI®). “Just Accepted” is an optional service offered to authors. Therefore, the “Just Accepted” Web site may not include all articles that will be published in the journal. After a manuscript is technically edited and formatted, it will be removed from the “Just Accepted” Web site and published as an ASAP article. Note that technical editing may introduce minor changes to the manuscript text and/or graphics which could affect content, and all legal disclaimers and ethical guidelines that apply to the journal pertain. ACS cannot be held responsible for errors or consequences arising from the use of information contained in these “Just Accepted” manuscripts.



# Light-Confining Nanoporous Anodic Alumina Microcavities by Apodized Stepwise Pulse Anodization

Cheryl Suwen Law<sup>1,2,3</sup>, Siew Yee Lim<sup>1,2,3</sup>, Raeanne M. Macalincag<sup>1</sup>, Andrew D. Abell<sup>2,3,4\*</sup>,  
and Abel Santos<sup>1,2,3\*</sup>

<sup>1</sup>School of Chemical Engineering, The University of Adelaide, SA 5005 Adelaide, Australia.

<sup>2</sup>Institute for Photonics and Advanced Sensing (IPAS), The University of Adelaide, SA 5005 Adelaide, Australia.

<sup>3</sup>ARC Centre of Excellence for Nanoscale BioPhotonics (CNBP), The University of Adelaide, SA 5005 Adelaide, Australia.

<sup>4</sup>Department of Chemistry, The University of Adelaide, SA 5005 Adelaide, Australia.

\*E-mails: [andrew.abell@adelaide.edu.au](mailto:andrew.abell@adelaide.edu.au) ; [abel.santos@adelaide.edu.au](mailto:abel.santos@adelaide.edu.au)

**KEYWORDS:** Nanoporous Anodic Alumina, Optical Microcavity, Light Confinement, Apodized Anodization, Quality Factor.

**ABSTRACT:** This study presents an innovative approach to fabricate nanoporous anodic alumina optical microcavities (NAA- $\mu$ CVs) with enhanced quality factor and versatile optical properties. An apodization strategy using a logarithmic negative function is applied to a stepwise pulse anodization process in order to engineer the effective medium of NAA so it confines light efficiently. The architecture of these light-trapping photonic crystals is composed of two highly reflecting mirrors with asymmetrically apodized effective medium. Various anodization parameters such as anodization time, anodization period, current density offset, and pore widening time are systematically modified to assess their effect on the optical properties of NAA- $\mu$ CVs in terms of quality factor and position of resonance band. We demonstrate that this fabrication approach enables the generation of NAA- $\mu$ CVs with high quality factor ( $\sim 113$ ) and well-resolved and tunable resonance bands across the spectral regions, from UV to NIR, through the manipulation of the anodization parameters. These results represent a comprehensive rationale for the development of high quality NAA- $\mu$ CVs with enhanced light-confining capabilities, providing new opportunities for further fundamental and applied research across a broad range of fields and disciplines such as photonics and optical sensing.

## INTRODUCTION

New materials and structures that effectively confine light to small volumes are central for the development and advancement of nanophotonic applications such as quantum communication and computing<sup>1</sup>, nanolasers<sup>2</sup>, ultra-small photonic filters<sup>3</sup>, and optical sensing.<sup>4</sup> Photons possess no charge or rest mass and are prone to escaping when trapped in photonic structures.<sup>5,6</sup> The confinement of light within small volumes comparable to the wavelength of light is challenging. However, high quality optical microcavities with strong light confinement capabilities to attain the precise control of light emission and propagation have been realized.<sup>7,8</sup> Photonic crystals (PCs) have emerged as the most promising platforms to develop efficient optical microcavities with high quality factor and small cavity volume.<sup>9,10</sup> Optical microcavities ( $\mu$ CVs) are photonic crystal structures that can guide and build up optical signals by light confinement.<sup>6</sup> Typically,  $\mu$ CVs consists of two plane-parallel mirrors positioned apart at a fixed distance with the objective of capturing and storing light indefinitely, until the system is triggered to release the confined light from the cavity in a controlled fashion.<sup>6,11,12</sup>  $\mu$ CVs can be produced in different materials, including polymers<sup>13</sup>, semiconductors such as GaAs, InP, GaInAsP and GaN<sup>14-17</sup> and silicon<sup>4,18,19</sup>. Usually,  $\mu$ CVs are fabricated by a combination of lithographic and etching techniques, and chemical or physical vapor deposition.<sup>17</sup> However, alternative materials such as porous silicon produced by electrochemical etching of silicon opened new opportunities to develop nanoporous  $\mu$ CVs with tunable optical properties and nanoporous architectures for different applications, including light-emitting devices, solar cells, optical filters, biosensors, drug delivery and theranostics.<sup>20-22</sup> The modulation of porosity in depth by the anodizing current allows the effective engineering the optical properties of porous silicon  $\mu$ CVs, the composite air-silicon matrix of which acts as a versatile effective medium.<sup>23-27</sup> Porous silicon has outstanding optoelectronic properties, however it has poor chemical stability and mechanical strength and

1  
2  
3 its fabrication process requires the use of extremely hazardous HF-based electrolytes.<sup>28,29</sup> To  
4  
5 date, different alternative/complementary nanoporous materials have been explored to  
6  
7 overcome the intrinsic limitations of porous silicon. Of these, nanoporous anodic alumina  
8  
9 (NAA) produced by anodization of aluminum has superior properties to those of porous  
10  
11 silicon in respect of mechanical, thermal and chemical stabilities as well as versatile nanopore  
12  
13 geometry. Furthermore, anodization of aluminum is a well-established electrochemical  
14  
15 process performed in mild acid electrolyte solutions that is economical and fully scalable  
16  
17 process and requires minimum safety measures.<sup>30-36</sup>

18  
19  
20 Recent studies have demonstrated that the effective refractive index of NAA can be  
21  
22 precisely modulated in a multi-dimensional fashion to create a broad range of PC structures  
23  
24 with finely tuned optical properties (e.g. distributed Bragg reflectors, gradient-index filters,  
25  
26 bandpass and linear variable bandpass filters, encoded photonic tags, etc.). The realization of  
27  
28 NAA-based  $\mu$ CVs has been demonstrated in a few pioneering studies.<sup>37-40</sup> The fabrication of  
29  
30 NAA- $\mu$ CVs involves the introduction of defect modes in the PC structure, which can be  
31  
32 achieved by various approaches such as the insertion of a thin layer of nanopores with  
33  
34 constant effective refractive index between two highly reflective Bragg mirrors, a phase shift  
35  
36 of effective refractive index between Bragg mirrors, or a progressive asymmetric modulation  
37  
38 of the effective medium in depth.<sup>37,38,41</sup> However, the maximum quality factors of NAA-  
39  
40  $\mu$ CVs reported by Wang *et al.* ( $\sim 24$ )<sup>38</sup>, Lee *et al.* ( $\sim 55$ )<sup>37</sup> and Yan *et al.* ( $\sim 45$ )<sup>41</sup> were found to  
41  
42 be significantly lower than those of porous silicon-based  $\mu$ CVs ( $\sim 1500-3400$ )<sup>19,42,43</sup> due to the  
43  
44 low refractive index of alumina ( $\text{Al}_2\text{O}_3 - n_{\text{Alumina}} \sim 1.70$ ).<sup>37-40</sup> Despite this limitation, the  
45  
46 development of new pulse-like anodization strategies and novel NAA-PC architectures  
47  
48 provides new opportunities to improve the quality of NAA- $\mu$ CVs and explore new strategies  
49  
50 to attain strong light confinements by a precise control of light-matter interactions at the  
51  
52 nanoscale.<sup>37-59</sup> Recently, we identified sharp resonance bands within the photonic stopband  
53  
54  
55  
56  
57  
58  
59  
60

(PSB) of NAA-PCs produced by stepwise pulse anodization when a logarithmic negative apodization function was applied under certain conditions.<sup>60</sup> Motivated by these results, we decided to explore this nanofabrication approach to develop high-quality NAA- $\mu$ CVs.

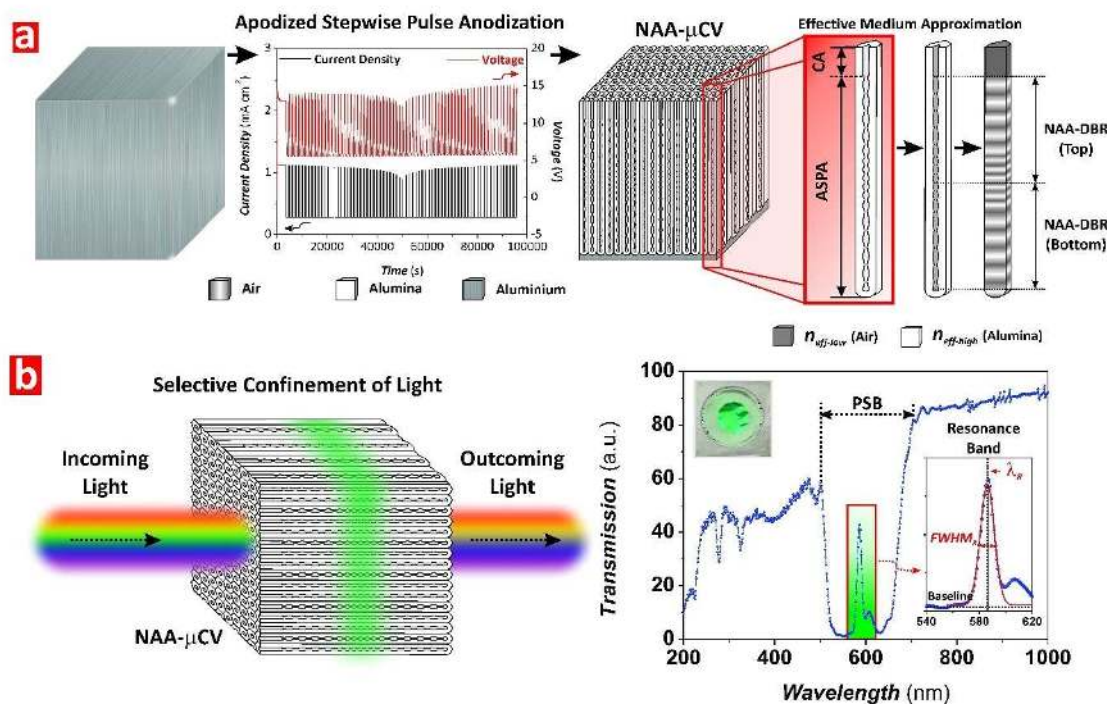


**Figure 1.** Fabrication of NAA- $\mu$ CVs by apodized stepwise pulse anodization (ASPA). a) Representative ASPA profile (left) and structure of NAA- $\mu$ CVs (right) showing details of the existing relationship between nanopore geometry and effective refractive index ( $n_{eff}$ ) distribution between high (alumina) and low (air) values along the nanopore depth. b) Schematic showing the confinement of light within the structure of NAA- $\mu$ CVs (left) and representative transmission spectra showing the characteristic photonic stopband (PSB) and the resonance band at its center in NAA- $\mu$ CVs. Insets show a digital picture of that NAA- $\mu$ CVs with the characteristic green interferometric color denoting the position of the photonic stopband and a magnified view of the red rectangle showing details of the resonance band (note: NAA- $\mu$ CV produced with  $T_p = 1300$  s,  $\Delta A_J = 0.210$  mA cm<sup>-2</sup>,  $J_{Offset} = 0.280$  mA cm<sup>-2</sup>,  $t_{An} = 25$  h, and  $t_{pw} = 6$  min).

In this study, a new architecture of NAA- $\mu$ CVs that enables high quality confinement of light by means of a rationally designed apodized stepwise pulse anodization (ASPA) approach is presented. A negative apodization function is implemented into the stepwise pulse anodization profile with the aim of modulating the effective refractive index of NAA in depth and engineering the photonic stopband (PSB) of the Bragg mirrors (**Figure 1**).<sup>61,62</sup> Various anodization parameters including anodization time, anodization period, current density offset, and pore widening time are systematically modified in order to maximize and

1  
2  
3 tune the resonance band of NAA- $\mu$ CVs across the spectral regions. Our study establishes a  
4 comprehensive rationale towards the fabrication of NAA- $\mu$ CVs with high quality factor and  
5 optimized optical properties. These PCs will enable new opportunities to expand the  
6 applicability of NAA- $\mu$ CVs across disciplines such as ultra-sensitive sensors, light  
7 harvesting/emitting devices, and optical filters.  
8  
9  
10  
11  
12

## 13 14 15 EXPERIMENTAL SECTION

16  
17 **2.1. Materials.** High purity (99.9997%) aluminum (Al) foils of thickness 0.32 mm were  
18 supplied by Goodfellow Cambridge Ltd. (UK). Sulfuric acid ( $\text{H}_2\text{SO}_4$ ), perchloric acid  
19 ( $\text{HClO}_4$ ), copper (II) chloride ( $\text{CuCl}_2$ ), hydrochloric acid (HCl), phosphoric acid ( $\text{H}_3\text{PO}_4$ ), and  
20 ethanol ( $\text{EtOH-C}_2\text{H}_5\text{OH}$ ) were supplied by Sigma-Aldrich (Australia) and used as received,  
21 without further purification steps. Aqueous solutions used in this study were prepared with  
22 Milli-Q® water ( $18.2 \text{ m}\Omega\cdot\text{cm}$ ).  
23  
24  
25  
26  
27  
28  
29

30 **2.2. Fabrication of Nanoporous Anodic Alumina Microcavities.** NAA optical  
31 microcavities (NAA- $\mu$ CVs) were produced by apodized stepwise pulse anodization (ASPA)  
32 under current density control conditions.  $1.5 \times 1.5 \text{ cm}$  Al square chips were cleaned under  
33 sonification in EtOH and Milli-Q® water for 15 min each, then dried under air stream. Prior  
34 to anodization, these Al substrates were electropolished in a mixture of EtOH and  $\text{HClO}_4$  4:1  
35 ( $v:v$ ) at 20 V and  $5^\circ\text{C}$  for 3 min. The anodization process of Al substrates was carried out in  
36 an electrochemical reactor at a constant temperature of  $-1^\circ\text{C}$ , using an aqueous solution of 1.1  
37 M  $\text{H}_2\text{SO}_4$  with 25  $v\%$  of EtOH as electrolyte. The galvanostatic anodization process started  
38 with a constant current density step at  $1.120 \text{ mA cm}^{-2}$  for 1 h to create a starting nanoporous  
39 oxide layer that acts a shuttle for achieving a homogenous pore growth rate preceding the  
40 ASPA step. The anodization profile was subsequently set to apodized stepwise pulse mode. A  
41 logarithmic negative apodization function was implemented into conventional stepwise pulse  
42  
43  
44  
45  
46  
47  
48  
49  
50  
51  
52  
53  
54  
55  
56  
57  
58  
59  
60

anodization. The current density-time ASPA profiles were produced by a custom-designed Labview®-based software according to **Equation 1**.

$$J(t) = 2A_J(t) + J_{offset} \quad (1)$$

where  $A_J(t)$  is the time-dependent current density amplitude, which follows a logarithmic negative apodization function as defined in **Equations 2 and 3**.

For  $t \leq t_{An}/2$

$$A(t)_J = A_{max} + \left( \frac{A_{min} - A_{max}}{\log\left(\frac{t_{An}}{2} + 10\right) - 1} \right) \cdot (\log(t + 10) - 1) \quad (2)$$

For  $t > t_{An}/2$

$$A(t)_J = \left( \frac{A_{max} - A_{min}}{\log(t_{An} + 10) - \log\left(\frac{t_{An}}{2} + 10\right)} \right) \cdot (\log(t + 10) - \log\left(\frac{t_{An}}{2} + 10\right)) + A_{min} \quad (3)$$

where  $A_{max}$  and  $A_{min}$  are the maximum and minimum amplitudes and  $t_{An}$  is the total anodization time at ASPA.

Note that  $T_P$  in the ASPA profile was defined as the total time length of high and low anodization current density pulses (**Equation 4**):

$$T_P = t_{high} + t_{low} \quad (4)$$

where  $t_{high}$  and  $t_{low}$  are the time duration at high and low current density values, respectively.

The ratio between  $t_{high}$  and  $t_{low}$  was set to  $t_{high}:t_{low} = 1:4$ .

To gain a better understanding of the light-confining capabilities of NAA- $\mu$ CVs produced by ASPA, different anodization parameters (i.e. anodization time  $-t_{An}$ , anodization period  $-T_P$ , current density offset  $-J_{offset}$ , and pore widening time  $-t_{pw}$ ) were systematically manipulated



to assess their effects on the optical characteristics of NAA- $\mu$ CVs, such as interferometric color, position of the resonance band ( $\lambda_R$ ), full-width at half maximum of the resonance band ( $FWHM_R$ ) and quality factor of cavity ( $Q_C$ ), as defined by **Equation 5**.

$$Q_C = \frac{\lambda_R}{FWHM_R} \quad (5)$$

**2.3. Optical Characterization.** Prior to optical characterization, the remaining aluminum substrate was selectively dissolved from the backside of these aluminum chips by wet chemical etching in a saturated solution of HCl/CuCl<sub>2</sub> using an etching cell with a Viton® mask with a circular window of 5 mm in diameter. These etched NAA- $\mu$ CVs were then optically characterized. The optical transmission spectra of NAA- $\mu$ CVs fabricated at various conditions were obtained at normal incidence (i.e.  $\theta = 0^\circ$ ) from 200–1000 nm with a resolution of 1 nm and 5 mm slit using a UV-vis-NIR spectrophotometer (Cary 60, Agilent, USA), and from 200–1500 nm with a resolution of 1 nm in a UV-vis-NIR spectrometer (UV-3600 Plus, Shimadzu, Japan). The interferometric color displayed by these NAA- $\mu$ CVs as a function of the different fabrication parameters was characterized through digital images acquired by a Canon EOS 700D digital camera equipped with a Tamron 90 mm F2.8 VC USD macro mount lens with autofocus function under natural illumination. A black card was used as background for the digital image acquisition. The pore size of NAA- $\mu$ CVs was widened by isotropic chemical etching in an aqueous solution of 5 wt% H<sub>3</sub>PO<sub>4</sub> at 35°C at different pore widening times (i.e.  $t_{pw} = 0, 2, 4,$  and 6 min) and their transmission spectra and digital images were recorded after each pore widening step. Note that the features of the resonance band of these NAA- $\mu$ CVs (i.e. position of resonance band  $-\lambda_R$ , full-width at half maximum of the resonance band  $-FWHM_R$ , and baseline of resonance band  $-y_0$ ) were estimated using OriginPro 8.5®, applying Gaussian fittings over the resonance bands shown in the transmission spectra of NAA- $\mu$ CVs and using as a baseline the lower lobe of the

1  
2  
3 photonic stopband (PSB), as illustrated in **Figure 1**. The obtained results were summarized in  
4  
5 contour maps generated using OriginPro 8.5®, using a triangulation algorithm in which the  
6  
7 coordinates of the intersection point were computed with linear interpolation.

8  
9 **2.4. Structural Characterization.** The nanoporous structure of NAA- $\mu$ CVs was  
10  
11 characterized by a field emission gun scanning electron microscope (FEG-SEM FEI Quanta  
12  
13 450). The obtained FEG-SEM images were analyzed using ImageJ (public domain program  
14  
15 developed at the RSB of the NIH).<sup>63</sup>

## 16 17 18 RESULTS AND DISCUSSION

### 19 20 **3.1. Fabrication and Structural Characterization of Nanoporous Anodic Alumina**

21  
22 **Microcavities.** **Figure 1a** illustrates the fabrication process of NAA- $\mu$ CVs by ASPA. The  
23  
24 structure of these PC structures is composed of two highly reflective distributed Bragg  
25  
26 reflector (DBR) mirrors with asymmetrically modulated effective refractive index in a  
27  
28 stepwise fashion in depth following a logarithmic negative window. The amplitude of the  
29  
30 current density pulse is logarithmically reduced during the fabrication process of the first half  
31  
32 of the NAA- $\mu$ CV (i.e. from  $t = 0$  to  $t = t_{An}/2$ ) (**Equation 2**). At  $t = t_{An}/2$ , the current density  
33  
34 amplitude is progressively increased according to the mathematical expression shown in  
35  
36 **Equation 3**. The transmission spectrum of these PC structures is characterized by a relatively  
37  
38 broad PSB with a strong and narrow resonance band at approximately its central position  
39  
40 (**Figure 1b**). This resonance band denotes a strong confinement of light within the NAA-  
41  
42  $\mu$ CV at that narrow range of wavelengths, which is established by the geometric features of  
43  
44 the NAA-DBR mirrors. **Figures 2a-c** show a set of representative FEG-SEM images of  
45  
46 NAA- $\mu$ CVs produced by ASPA. These images reveal that the structure of these PCs is  
47  
48 composed of stacked layers of NAA with a porosity modulation in depth that follows the  
49  
50 ASPA current density profile applied during the anodization process. **Figure 2a** depicts a  
51  
52  
53  
54  
55  
56  
57  
58  
59  
60

representative top view FEG-SEM image of a NAA- $\mu$ CV, revealing nanopores with an average pore diameter ( $d_p$ ) of  $15 \pm 2$  nm that are randomly distributed across the surface.

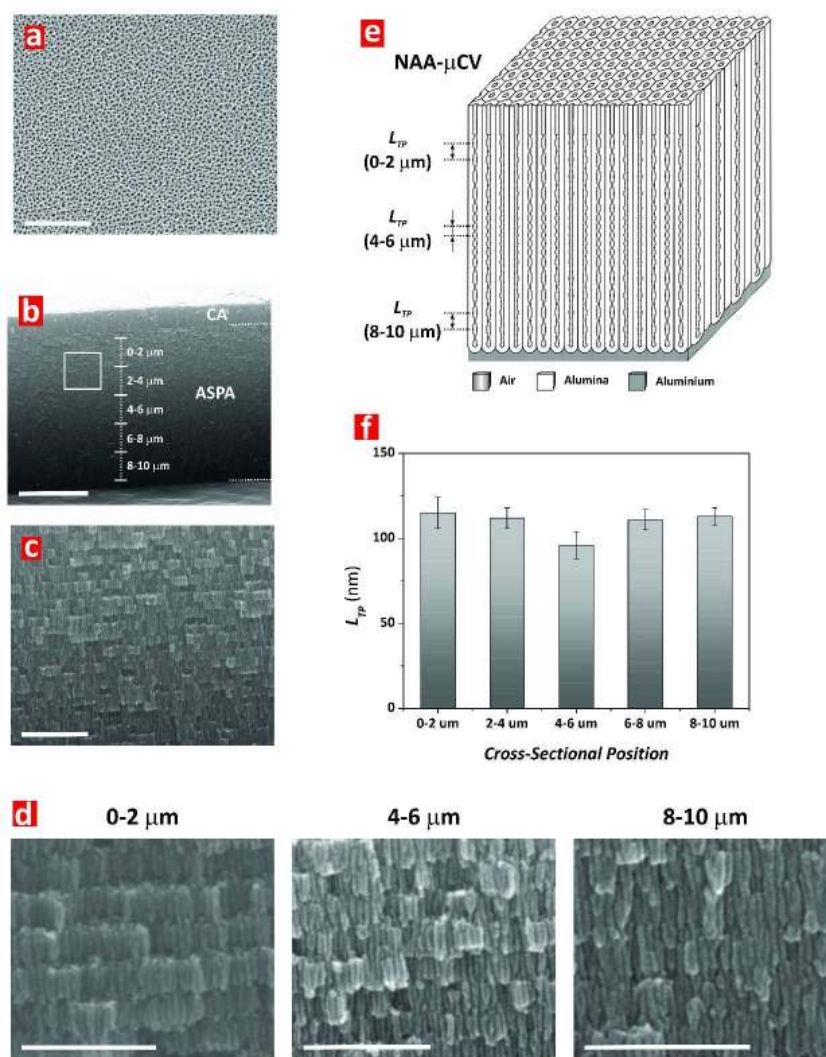


**Figure 2.** Nanoporous structure of NAA- $\mu$ CVs produced by ASPA. a) Representative top view FEG-SEM image of a NAA- $\mu$ CV showing a random distribution of nanopores with  $d_p = 15 \pm 2$  nm (scale bar = 500 nm). b) General cross-sectional view FEG-SEM image of a NAA- $\mu$ CV showing a top layer of straight nanopore diameter (constant anodization = CA – thickness =  $1.4 \pm 0.1$   $\mu$ m) and the PC microcavity layer with nanopore diameter modulation (ASPA – thickness =  $11.0 \pm 0.1$   $\mu$ m) with details showing the areas where the period length ( $L_{TP}$ ) was estimated (i.e. from 0-2  $\mu$ m to 8-10  $\mu$ m) (scale bar = 5  $\mu$ m). c) Magnified view of the white rectangle shown in (b) revealing the porosity modulation in depth in NAA- $\mu$ CVs (scale bar = 1  $\mu$ m). d) Magnified views at different cross-sectional positions (i.e. 0-2, 4-6, and 8-10  $\mu$ m) showing details of the period length modulation (scale bar = 500 nm). e) Illustration representing the idealized nanoporous structure of NAA- $\mu$ CVs, where the period length ( $L_{TP}$ ) is modified in depth to create an optical microcavity structure with a logarithmically modulated effective refractive index composed of two NAA-DBRs with asymmetrically modulated effective refractive index. f) Bar chart showing the period length distribution in NAA- $\mu$ CVs produced by ASPA along the nanopore depth (note: NAA- $\mu$ CV produced with  $T_p = 800$  s,  $\Delta A_j = 0.210$  mA cm $^{-2}$ ,  $J_{Offset} = 0.280$  mA cm $^{-2}$ ,  $t_{An} = 20$  h, and  $t_{pw} = 6$  min).

**Figure 2b** shows a general cross-sectional view of a NAA- $\mu$ CV produced with  $T_P = 800$  s,  $J_{offset} = 0.280$  mA cm $^{-2}$ ,  $\Delta A_J = 0.210$  mA cm $^{-2}$ ,  $t_{An} = 10$  h, and  $t_{pw} = 6$  min. That image reveals that the structure of these NAA- $\mu$ CVs is composed of a top layer  $1.4 \pm 0.1$   $\mu$ m thick with constant nanopore diameter, which results from the first anodization stage at constant anodizing current density (CA –  $J = 1.120$  mA cm $^{-2}$  for 1 h), and a much thicker layer (i.e.  $11.0 \pm 0.1$   $\mu$ m) with nanopore diameter modulation in depth corresponding to the ASPA stage (**Figures 2c and d**). A pore branching effect can be observed at the bottom part of the NAA- $\mu$ CV structure (**Figure 2d**; 8-10  $\mu$ m), which can be associated with the non-self-organization conditions used in our study. A closer analysis of the period length (i.e.  $L_{TP}$  – distance between adjacent layers in the ASPA section of the NAA- $\mu$ CVs) reveals a direct dependency with the anodization amplitude ( $\Delta A_J$ ) (**Figure 2e**). For instance, we estimated the average  $L_{TP}$  along the ASPA cross-section of a NAA- $\mu$ CV produced with  $T_P = 800$  s,  $J_{offset} = 0.280$  mA cm $^{-2}$ ,  $\Delta A_J = 0.210$  mA cm $^{-2}$ ,  $t_{An} = 10$  h, and  $t_{pw} = 6$  min every 2  $\mu$ m by FEG-SEM image analysis. Our results indicate that  $L_{TP}$  varies along the nanopore depth following the apodization function applied during anodization, with an estimation of  $115 \pm 9$  nm at 0–2  $\mu$ m,  $112 \pm 6$  nm at 2–4  $\mu$ m,  $96 \pm 8$  nm at 4–6  $\mu$ m,  $111 \pm 6$  nm at 6–8  $\mu$ m, and  $113 \pm 5$  nm at 8–10  $\mu$ m (**Figure 2f**). From this analysis it is apparent that  $L_{TP}$  is reduced at the center of the ASPA section of the NAA- $\mu$ CVs (i.e.  $t \sim t_{An}/2$ ), which is expected due to the significant reduction of the anodization amplitude at  $t = t_{An}/2$ . Furthermore, FEG-SEM image analysis denote a modulation of porosity in depth with the pulse anodizing current density. For instance, the porosity at  $J = 0.280$  and  $1.120$  mA cm $^{-2}$  (i.e. minimum and maximum values of current density) was estimated to be  $18 \pm 9$  and  $32 \pm 13\%$ , respectively.<sup>48</sup> Apodization is a filtering technique broadly used in optics to narrow the PSB of photonic structures. The direct relationship between the geometric features of NAA- $\mu$ CVs and the anodization parameters

enables the apodization of the optical signals of these PCs by structural engineering of their effective medium (i.e. effective refractive index modulation).

### 3.2. Effect of Anodization Time ( $t_{An}$ ) on the Optical Properties of Nanoporous Anodic Alumina Microcavities.

To understand the effect of  $t_{An}$  on the optical characteristics of NAA- $\mu$ CVs, a set of NAA- $\mu$ CVs was fabricated using logarithmic negative ASPA with varying  $t_{An}$  from 5 to 25 h at an interval of 5 h. Other anodization parameters such as anodization period ( $T_P$ ), current density offset ( $J_{offset}$ ), and amplitude difference ( $\Delta A_J$ ) were fixed at 1200 and 1300 s, 0.280 mA cm<sup>-2</sup>, and 0.210 mA cm<sup>-2</sup>, respectively. **Figures 3a and b** show representative anodization profiles for NAA- $\mu$ CVs fabricated at different  $t_{An}$  (i.e. 5, 10, 15, 20, and 25 h) for  $T_P = 1200$  and 1300 s, respectively. These ASPA profiles denote that, under the anodization conditions used in our study, the anodizing current density profile is precisely translated into modulations of voltage throughout the whole process, resulting in an internal modulation of  $d_p$  in depth. The transmission spectra of NAA- $\mu$ CVs produced at  $T_P = 1300$  s as a function of  $t_{An}$  and pore widening time ( $t_{pw}$ ) are displayed in **Figures 4a-e**. The optical properties of these NAA- $\mu$ CVs were characterized in terms of  $\lambda_R$ ,  $FWHM_R$ ,  $Q_c$ , and interferometric color. **Figure 4** shows that the PSB of these NAA- $\mu$ CVs is located within visible-NIR range and it undergoes a blue shift and increases its intensity and width with  $t_{pw}$ , from 0 to 6 min. The interferometric color is a result of the selective and constructive reflection of light by the NAA- $\mu$ CV structure and denotes the position of the PSB within the UV (transparent), visible (color), or NIR (transparent) spectral regions. The transmission spectra of these NAA- $\mu$ CVs shows a resonance band located at approximately the center of the PSB, which indicates the presence of an optical microcavity within the structure of these PCs.

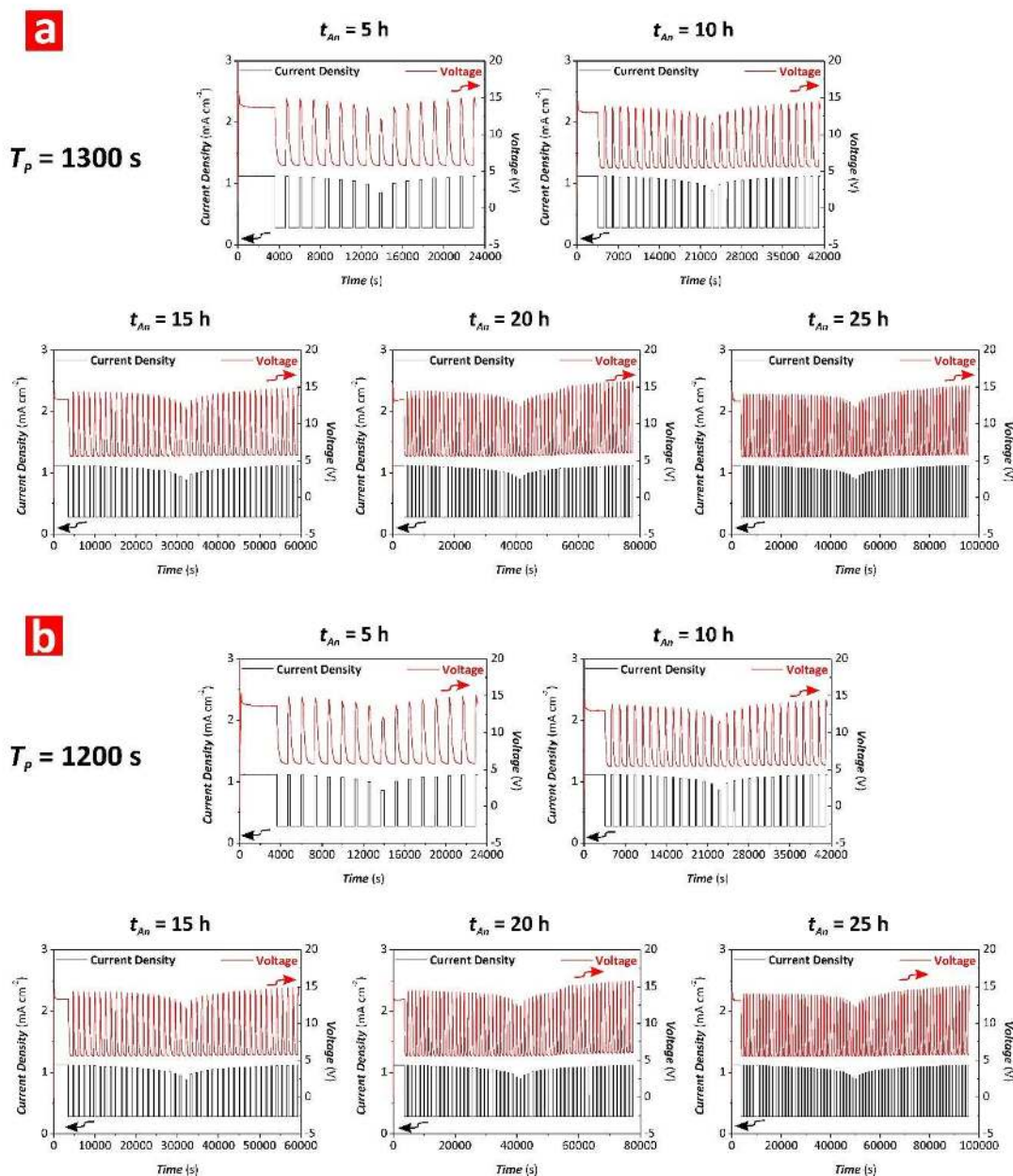


**Figure 3.** Representative anodization profiles of NAA- $\mu$ CVs produced by ASPA at different anodization times and anodization periods (note: NAA- $\mu$ CVs produced with  $T_p = 1200$  and  $1300$  s,  $\Delta A_J = 0.210$  mA cm $^{-2}$  and  $J_{Offset} = 0.280$  mA cm $^{-2}$ ). a) Anodization profiles of NAA- $\mu$ CVs produced with  $T_p = 1300$  at  $t_{An} = 5, 10, 15, 20,$  and  $25$  h. b) Anodization profiles of NAA- $\mu$ CVs produced with  $T_p = 1200$  at  $t_{An} = 5, 10, 15, 20,$  and  $25$  h.

**Figures 5a-e** show magnified views of the resonance bands observed in the transmission spectra of these NAA- $\mu$ CVs (**Figures 4a-e**) with details of Gaussian fittings used to estimate  $\lambda_R$ ,  $FWHM_R$ , and  $Q_C$ . In general, it can be observed that the resonance band of these NAA-



$\mu$ CVs rises as  $t_{pw}$  increases, becoming more well-resolved and intense due to the effective refractive index contrast enhancement between adjacent NAA layers.

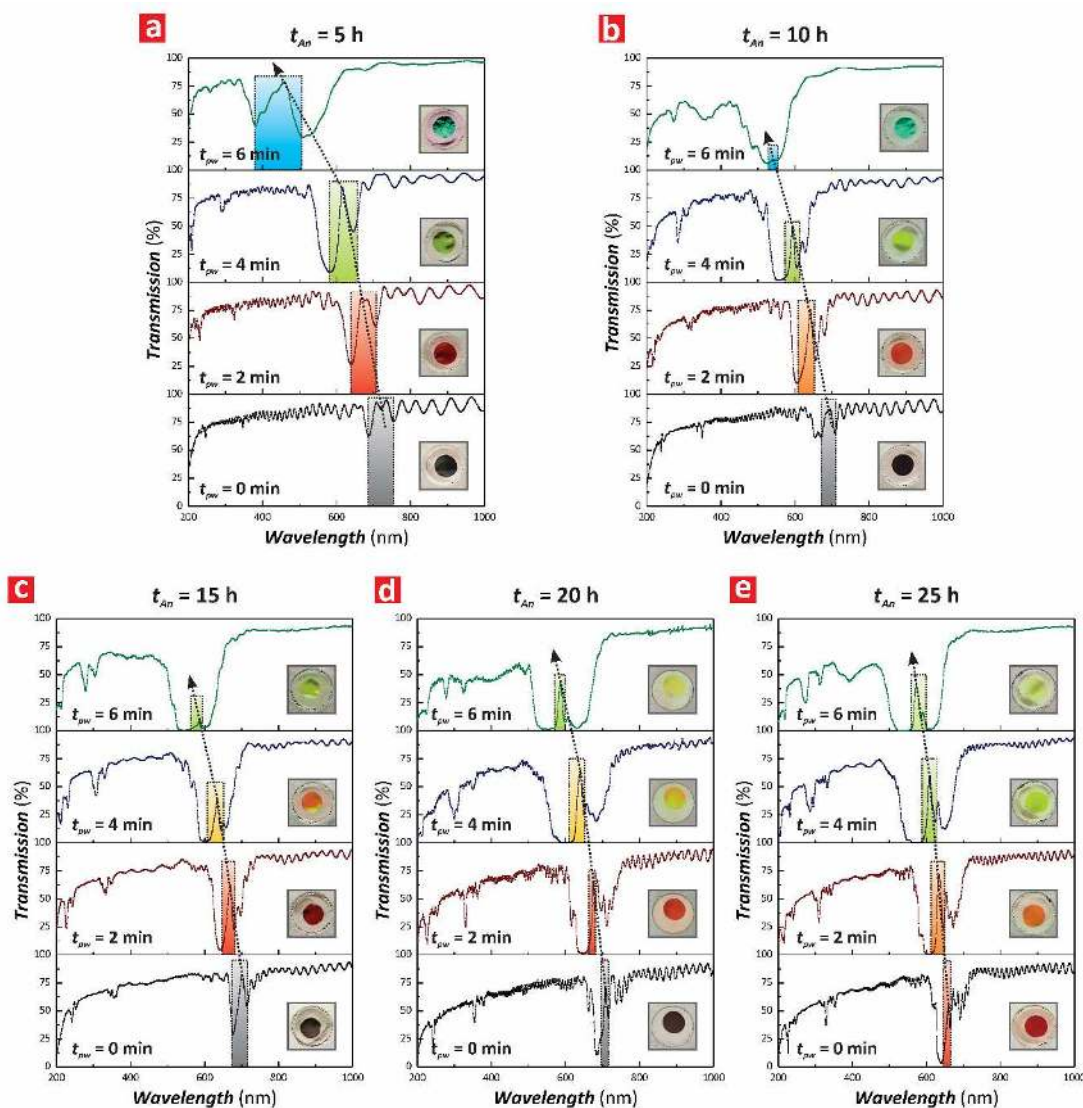


**Figure 4.** Combinational effect of anodization time ( $t_{An}$ ) and pore widening time ( $t_{pw}$ ) on the transmission spectrum of NAA- $\mu$ CVs produced by ASPA at  $T_p = 1300$  s (note: color rectangles denote the approximate position of the resonance band within the PSB and black dotted arrow lines indicate the blue shift of the resonance bands with  $t_{pw}$ ). a)  $t_{An} = 5$ , b)  $t_{An} = 10$ , c)  $t_{An} = 15$ , d)  $t_{An} = 20$ , and e)  $t_{An} = 25$  h. Insets in a-e display digital pictures of these photonic crystal structures showing vivid interferometric colors when the resonance band is located within the visible region and transparent when the band is within the UV or NIR spectral regions.

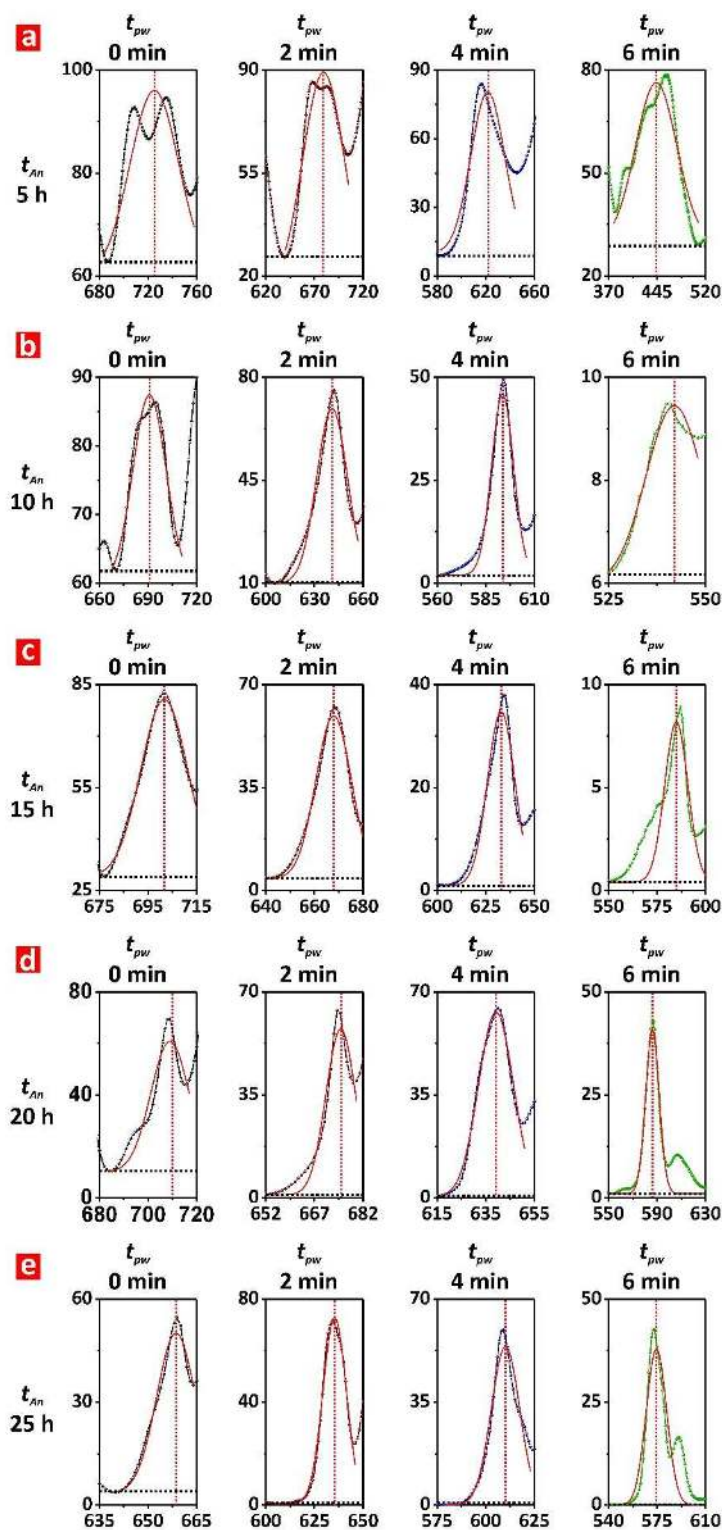


**Figure 5.** Combinational effect of anodization time ( $t_{An}$ ) and pore widening time ( $t_{pw}$ ) on the resonance band of NAA- $\mu$ CVs produced by ASPA at  $T_p = 1300$  s (note: horizontal dotted black lines denote the baseline ( $y_0$ ) used for the Gaussian fittings, which correspond to the lower lobe of the PSB, and vertical dotted red lines indicate the central wavelength of the resonance band ( $\lambda_R$ ) and the symmetry of the Gaussian fitting). a)  $t_{An} = 5$ , b)  $t_{An} = 10$ , c)  $t_{An} = 15$ , d)  $t_{An} = 20$ , and e)  $t_{An} = 25$  h.



1  
2  
3 The stepwise modulation of nanopores within NAA- $\mu$ CVs is more evident as the nanoporous  
4 structure of NAA is chemically etched, since those layers produced at lower anodizing  
5 current density dissolve at a faster rate than those produced at higher  $J$  (**Figure S1 –**  
6  
7 **Supporting Information**). However, the over-etching of the NAA- $\mu$ CVs' structure ( $t_{pw} > 4$   
8 min) results in a broadening of the resonance band and a decrement of its intensity due to  
9 light scattering by the overall PC structure (**Figure S2 – Supporting Information**). So, for  
10 NAA- $\mu$ CVs produced at  $t_{An} = 5, 10, \text{ and } 15$  h, the resonance band is almost vanished from the  
11 transmission spectrum at  $t_{pw} = 6$  min. To further extend the analysis on the effect of  $t_{An}$  on the  
12 optical properties of NAA- $\mu$ CVs produced by ASPA, we fabricated another set of NAA-  
13  $\mu$ CVs under the same conditions (i.e.  $J_{offset} = 0.280 \text{ mA cm}^{-2}$ ,  $\Delta A_J = 0.210 \text{ mA cm}^{-2}$ , and  $t_{An} =$   
14 5, 10, 15, 20, and 25 h) but setting the anodization period at  $T_P = 1200$  s. **Figure 3b** shows  
15 representative anodization profiles of these NAA- $\mu$ CVs produced at  $T_P = 1200$  s, showing  
16 how the anodizing current density (input) is directly translated into voltage (output) changes  
17 in a dynamic fashion, without apparent delay. **Figures 6a-e** show the transmission spectra of  
18 NAA- $\mu$ CVs produced with  $T_P = 1200$  s, which also include digital pictures displaying the  
19 characteristic interferometric color of these PC structures. As these graphs indicate, the PSB  
20 of these NAA- $\mu$ CVs is located within the visible-NIR region of the spectrum, although  
21 slightly blue-shifted as compared to their  $T_P = 1300$  s counterparts. As demonstrated in  
22 previous studies, this blue shift is associated with the reduction of the anodization period,  
23 which results in a shorter period length ( $L_{TP}$ ) within the nanoporous structure of NAA-  
24  $\mu$ CVs.<sup>43-59</sup> The transmission spectra of these NAA- $\mu$ CVs displays a PSB that increases its  
25 intensity with  $t_{pw}$  and a well-defined resonance band at the center of the PSB. **Figures 7a-e**  
26 compile magnified views of the resonance bands observed in the transmission spectra of  
27 these NAA- $\mu$ CVs (**Figures 6a-e**), with details of Gaussian fittings used to estimate  $\lambda_R$ ,  
28  $FWHM_R$ , and  $Q_c$ .

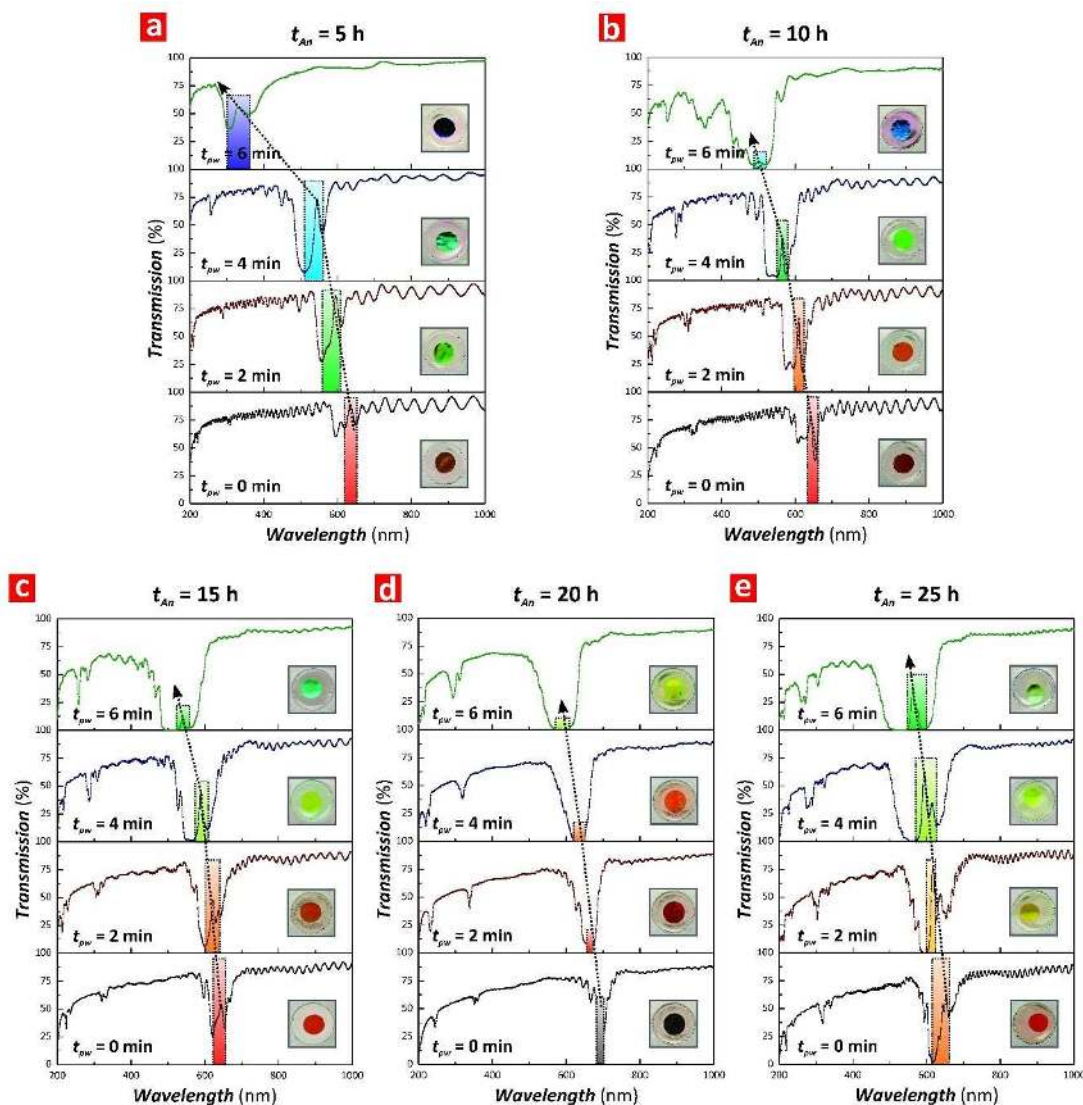


**Figure 6.** Combinational effect of anodization time ( $t_{An}$ ) and pore widening time ( $t_{pw}$ ) on the transmission spectrum of NAA- $\mu$ CVs produced by ASPA at  $T_P = 1200$  s (note: color rectangles denote the approximate position of the resonance band within the PSB and black dotted arrow lines indicate the blue shift of the resonance bands with  $t_{pw}$ ). a)  $t_{An} = 5$ , b)  $t_{An} = 10$ , c)  $t_{An} = 15$ , d)  $t_{An} = 20$ , and e)  $t_{An} = 25$  h. Insets in a-e display digital pictures of these photonic crystal structures showing vivid interferometric colors when the resonance band is located within the visible region and transparent when the band is within the UV or NIR spectral regions.

The quality factor ( $Q_C$ ), defined as the ratio of the resonance band wavelength ( $\lambda_R$ ) to its full width at half maximum ( $FWHM_R$ ) (Equation 5), is an important criteria in assessing the strength of photon confinement within optical microcavities.<sup>64,65</sup> The  $Q_C$  of these NAA- $\mu$ CVs was estimated by fitting the resonance bands shown in Figures 5 and 7 to Gaussian envelopes, using as a baseline the lower lobe of the PSB as indicated by the horizontal dotted black lines showed in these graphs.

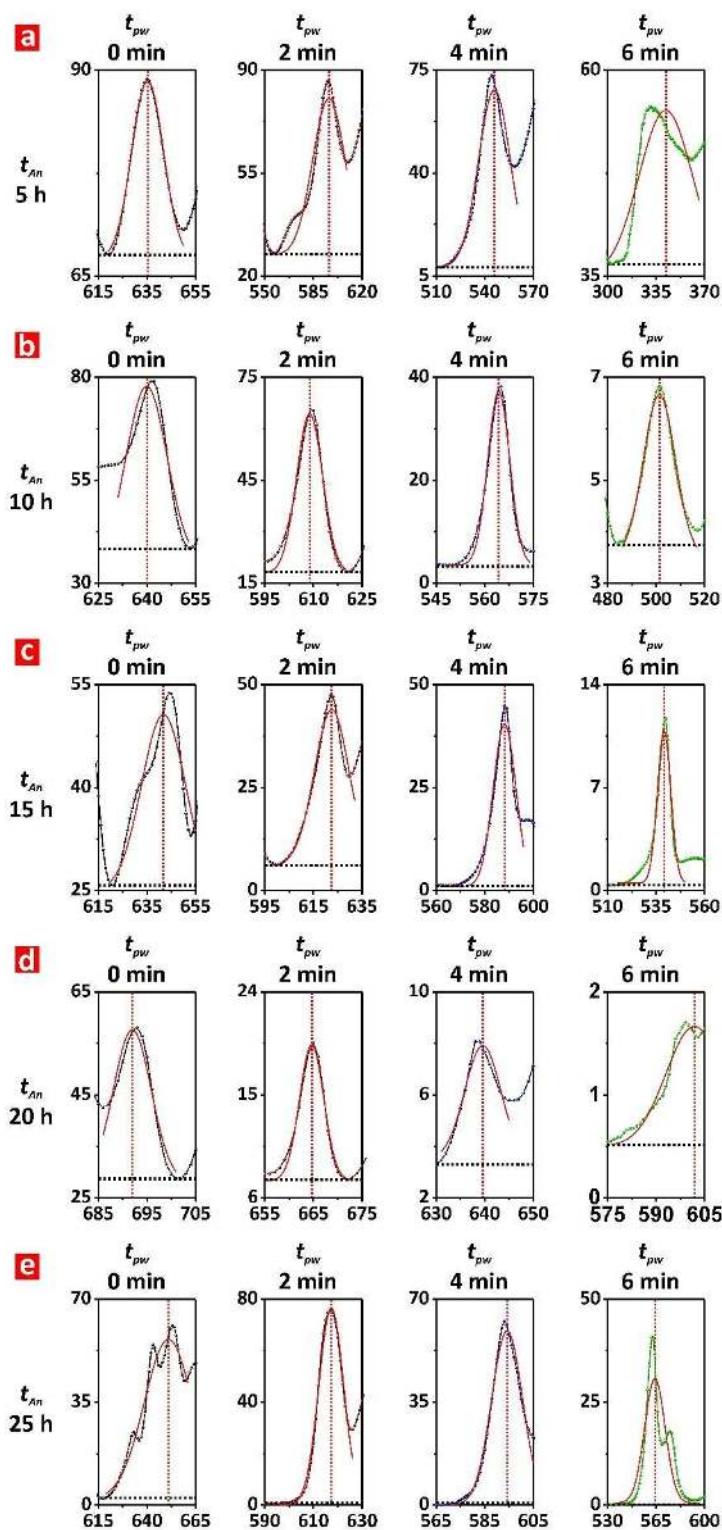


**Figure 7.** Combinational effect of anodization time ( $t_{An}$ ) and pore widening time ( $t_{pw}$ ) on the resonance band of NAA- $\mu$ CVs produced by ASPA at  $T_p = 1200$  s (note: horizontal dotted black lines denote the baseline ( $y_0$ ) used for the Gaussian fittings, which correspond to the lower lobe of the PSB, and vertical dotted red lines indicate the central wavelength of the resonance band ( $\lambda_R$ ) and the symmetry of the Gaussian fitting). a)  $t_{An} = 5$ , b)  $t_{An} = 10$ , c)  $t_{An} = 15$ , d)  $t_{An} = 20$ , and e)  $t_{An} = 25$  h.

1  
2  
3 A summary of the estimated values of  $y_0$ ,  $\lambda_R$ ,  $FWHM_R$  and  $Q_C$  are compiled in **Tables S1-S3**  
4  
5 **(Supporting Information)** along with the quality ( $R^2$ ) of these Gaussian fittings. **Figure 8**  
6  
7 shows contour maps summarizing the dependency of  $Q_C$  and  $\lambda_R$  with  $t_{An}$  and  $t_{pw}$  for NAA-  
8  
9  $\mu$ CVs produced with  $T_P = 1200$  and  $1300$  s,  $J_{offset} = 0.280$  mA cm<sup>-2</sup>, and  $\Delta A_J = 0.210$  mA cm<sup>-2</sup>.  
10  
11 **Figure 8a** shows the dependency of  $Q_C$  on  $t_{An}$  and  $t_{pw}$  for NAA- $\mu$ CVs fabricated with  $T_P =$   
12  
13  $1300$  s. It is apparent that  $Q_C$  becomes more dependent on these fabrication parameters at  
14  
15 short pore widening times (i.e. from  $t_{pw} = 0$  to  $2$  min) and longer anodization times (i.e. from  
16  
17  $t_{An} = 15$  to  $25$  h). This trend is denoted by a closer and denser concentration of color fields  
18  
19 around the  $Q_C$  maximum (i.e.  $Q_C = 63.1 \pm 1.2$ ), which is located at  $t_{pw} = 2$  min and  $t_{An} = 20$  h.  
20  
21 In general, an increase in  $t_{An}$  leads to an enhancement of the  $Q_C$  of NAA- $\mu$ CVs, while longer  
22  
23 pore widening times worsen the quality factor of the NAA- $\mu$ CVs. The relationship between  
24  
25  $\lambda_R$  with  $t_{An}$  and  $t_{pw}$  for NAA- $\mu$ CVs produced with  $T_P = 1300$  s is displayed in **Figure 8b**,  
26  
27 where it can be clearly observed that the distance between color fields is closer as  $t_{An}$  is  
28  
29 reduced from  $10$  to  $5$  h. This indicates a strong dependency of  $\lambda_R$  with  $t_{An}$  at shorter  
30  
31 anodization times. Furthermore, it is observed that  $\lambda_R$  is blue-shifted with  $t_{pw}$  across the UV-  
32  
33 visible spectrum from  $t_{An} = 5$  to  $25$  h. This analysis also reveals that the effect of  $t_{An}$  on the  
34  
35 position of the resonance band is not as significant as that of  $t_{pw}$ , since only a slight red shift  
36  
37 is observed as  $t_{An}$  increases from  $5$  to  $20$  h, and a slight blue shift from  $20$  to  $25$  h, achieving  
38  
39 its maximum value (i.e.  $725 \pm 1$  nm) at  $t_{An} = 5$  h and  $t_{pw} = 0$  min. The distribution of  $Q_C$  and  $\lambda_R$   
40  
41 for NAA- $\mu$ CVs produced at  $T_P = 1200$  s with  $t_{An}$  and  $t_{pw}$  is presented in **Figures 8c and d**,  
42  
43 respectively. The contour map shown in **Figure 8c** reveals a concentration of color fields at  
44  
45 the region of longer  $t_{An}$  and shorter  $t_{pw}$ , achieving a local maximum of  $Q_C$  (i.e.  $112.6 \pm 5.2$ ) at  
46  
47  $t_{An} = 20$  h and  $t_{pw} = 2$  min, which is the highest quality factor reported for a NAA-based  
48  
49 optical microcavity to date.  
50  
51  
52  
53  
54  
55  
56  
57  
58  
59  
60

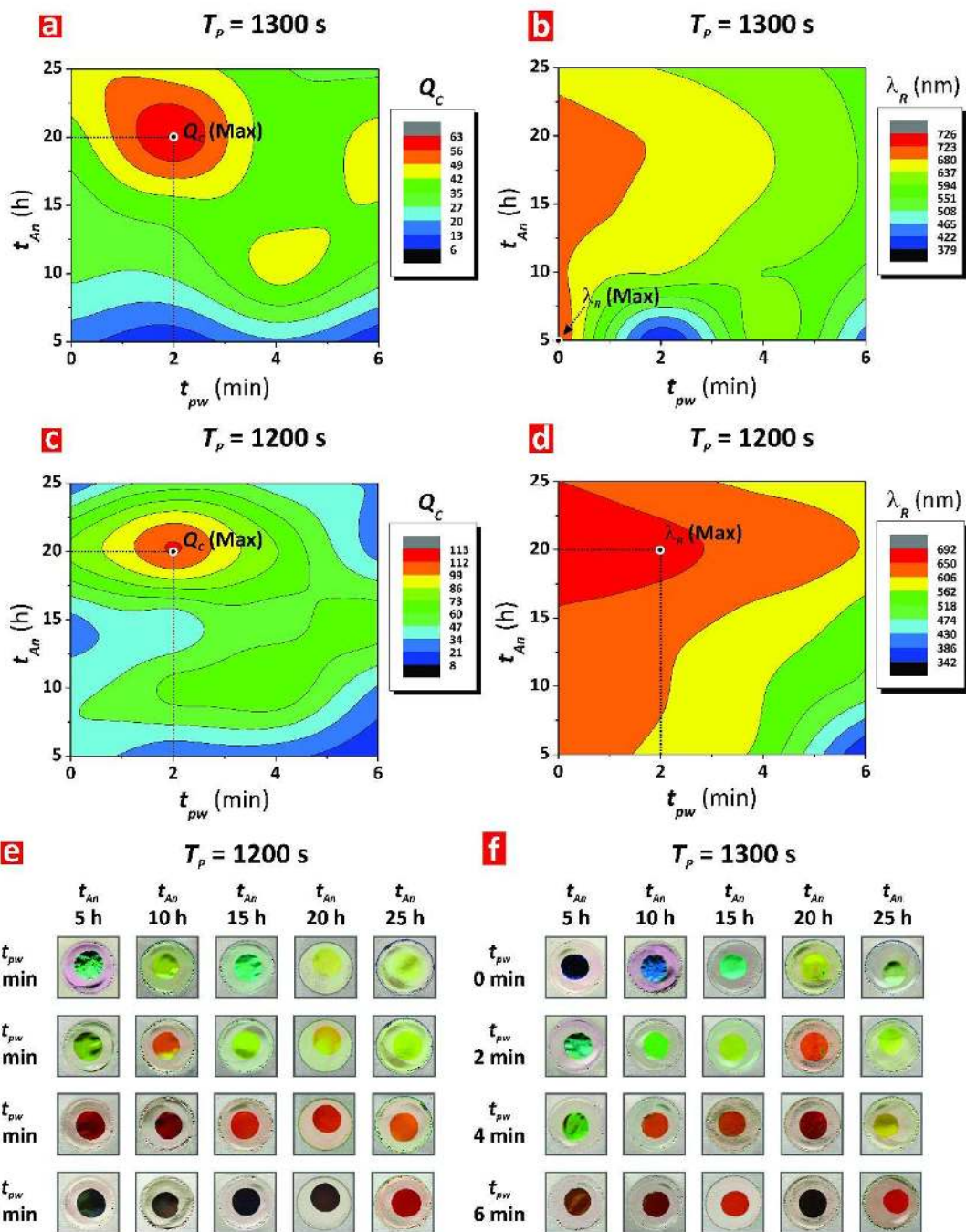


**Figure 8.** Combinational effect of anodization time ( $t_{An}$ ) and pore widening time ( $t_{pw}$ ) on the optical properties of NAA- $\mu$ CVs (i.e. quality factor –  $Q_C$ , position of resonance band –  $\lambda_R$ , and interferometric color) produced by ASPA. a) Contour map showing the dependency of  $Q_C$  with  $t_{An}$  and  $t_{pw}$  for NAA- $\mu$ CVs produced with  $T_p = 1300$  s. b) Contour map showing the dependency of  $\lambda_R$  with  $t_{An}$  and  $t_{pw}$  for NAA- $\mu$ CVs produced with  $T_p = 1300$  s. c) Contour map showing the dependency of  $Q_C$  with  $t_{An}$  and  $t_{pw}$  for NAA- $\mu$ CVs produced with  $T_p = 1200$  s. d) Contour map showing the dependency of  $\lambda_R$  with  $t_{An}$  and  $t_{pw}$  for NAA- $\mu$ CVs produced with  $T_p = 1200$  s. e) Digital images showing the interferometric color displayed by NAA- $\mu$ CVs produced with  $T_p = 1200$  s as a function of  $t_{An}$  and  $t_{pw}$ . f) Digital images showing the interferometric color displayed by NAA- $\mu$ CVs produced with  $T_p = 1300$  s as a function of  $t_{An}$  and  $t_{pw}$ .



1  
2  
3 The distance between field lines around the local maximum is shorter, indicating a stronger  
4 dependency of  $Q_C$  on  $t_{An}$  and  $t_{pw}$  around that set of fabrication conditions. In contrast, the  
5 combination of shorter  $t_{An}$  (i.e. 5 to 15 h) and longer  $t_{pw}$  (i.e. 4 to 6 min) worsens  $Q_C$  as the  
6 distance between field lines and color fields is relatively broad at these areas. **Figure 8d**  
7 shows how  $t_{An}$  and  $t_{pw}$  affect  $\lambda_R$  of NAA- $\mu$ CVs produced at  $T_P = 1200$  s. This graph denotes a  
8 homogenous but broad distribution of color fields with equidistant field lines throughout,  
9 from  $t_{An} = 5$  to 25 h and from  $t_{pw} = 0$  to 4 min, which indicates a weak dependency of  $\lambda_R$  on  $t_{An}$   
10 and  $t_{pw}$  at these combinations of fabrication parameters. As  $t_{pw}$  increases from 4 to 6 min and  
11  $t_{An}$  decreases from 10 to 5 h,  $\lambda_R$  shows a stronger dependency with these parameters, as  
12 suggested by the closer field lines and high density of color fields.  $\lambda_R$  is red-shifted as  $t_{An}$   
13 increases from 5 to 20 h and slightly blue-shifted when  $t_{An}$  increases from 20 to 25 h. The  
14 maximum value of  $\lambda_R$  (i.e.  $665 \pm 1$  nm) is achieved at  $t_{An} = 20$  h and  $t_{pw} = 2$  min. Furthermore,  
15 this analysis also reveals that  $t_{pw}$  blue-shifts the resonance band of NAA- $\mu$ CVs produced at  
16  $T_P = 1200$  s as  $t_{pw}$  increases. The comparative analysis of **Figures 8a and c** reveals that a  
17 combination of long  $t_{An}$  (i.e. from 15 to 25 h) and short  $t_{pw}$  (i.e. from 0 to 2 min) results in  
18 high quality NAA- $\mu$ CVs with narrow and well-resolved resonance bands. The average  $Q_C$   
19 estimated for NAA- $\mu$ CVs produced with  $T_P = 1200$  and 1300 s were  $46.4 \pm 24.8$  and  $33.7 \pm$   
20  $13.8$ , respectively. It is worthwhile noting that only one of the NAA- $\mu$ CVs produced at 1300  
21 s showed superior light-confining performance than those reported in previous studies (i.e.  
22  $Q_C = 63.1 \pm 1.2$  for NAA- $\mu$ CV produced with  $T_P = 1300$  s,  $t_{pw} = 2$  min and  $t_{An} = 20$  h – Wang  
23 *et al.* ( $\sim 24$ )<sup>38</sup>, Lee *et al.* ( $\sim 55$ )<sup>37</sup> and Yan *et al.* ( $\sim 45$ )<sup>41</sup>). However, up to six NAA- $\mu$ CVs  
24 produced with  $T_P = 1200$  s showed superior properties to confine light than previously NAA-  
25 based optical microcavities (i.e.  $Q_C = 64.0 \pm 1.0$  at  $t_{pw} = 2$  min and  $t_{An} = 10$  h,  $Q_C = 70.5 \pm 2.1$   
26 at  $t_{pw} = 4$  min and  $t_{An} = 10$  h,  $Q_C = 66.0 \pm 1.3$  at  $t_{pw} = 6$  min and  $t_{An} = 15$  h,  $Q_C = 75.2 \pm 3.1$  at  
27  $t_{pw} = 0$  min and  $t_{An} = 20$  h,  $Q_C = 112.6 \pm 5.2$  at  $t_{pw} = 2$  min and  $t_{An} = 20$  h, and  $Q_C = 73.5 \pm 2.6$   
28  
29  
30  
31  
32  
33  
34  
35  
36  
37  
38  
39  
40  
41  
42  
43  
44  
45  
46  
47  
48  
49  
50  
51  
52  
53  
54  
55  
56  
57  
58  
59  
60

1  
2  
3 at  $t_{pw} = 4$  min and  $t_{An} = 20$  h). Although both types of NAA- $\mu$ CVs have a weak correlation  
4  
5 between the shift in  $\lambda_R$  with  $t_{An}$ , **Figures 8b and d** show that the  $\lambda_R$  of NAA- $\mu$ CVs produced  
6  
7 at  $T_P = 1300$  s evolves in a slightly different manner with  $t_{An}$  as compared to NAA- $\mu$ CVs  
8  
9 fabricated at  $T_P = 1200$  s. This graph also indicates that, as observed in the transmission  
10  
11 spectra (**Figures 4 and 6**) the position of the PSB and resonance bands of NAA- $\mu$ CVs  
12  
13 produced at  $T_P = 1200$  s is blue-shifted as compared to their equivalent NAA- $\mu$ CVs  
14  
15 fabricated at  $T_P = 1300$  s. It is also observed that both sets of NAA- $\mu$ CVs show a stronger  
16  
17 dependency of  $\lambda_R$  with  $t_{pw}$  than that shown for  $t_{An}$ . A pore widening treatment blue-shifts the  
18  
19 position of the respective resonance bands, and the longer  $t_{pw}$  is, the shorter the wavelength  
20  
21 where the resonance band is positioned at. It is worthwhile to note that, for a given  $t_{pw}$ , the  
22  
23 position of the resonance band of NAA- $\mu$ CVs at  $T_P = 1300$  s is located at longer wavelengths  
24  
25 than that of NAA- $\mu$ CVs produced with  $T_P = 1200$  s due to the red shift associated with the  
26  
27 longer anodization period and longer period length. Another interesting optical property of  
28  
29 NAA- $\mu$ CVs is their vivid interferometric colors, which correspond to the wavelength of their  
30  
31 respective PSB and  $\lambda_R$  when these are positioned within the visible range of the spectrum.  
32  
33 **Figures 8e and f** compile digital images of NAA- $\mu$ CVs produced at  $T_P = 1200$  and  $1300$  s as  
34  
35 a function of  $t_{An}$  and  $t_{pw}$ , respectively. The analysis of these images is in good agreement with  
36  
37 the results obtained in **Figures 8b and d**, where the  $\lambda_R$  is blue-shifted with  $t_{pw}$ . It is also  
38  
39 apparent that  $\lambda_R$  is red-shifted with increasing  $t_{An}$  from 5 to 20 h and slightly blue shifted from  
40  
41  $t_{An} = 20$  to 25 h.

42  
43  
44  
45  
46  
47  
48 **3.3. Effect of Anodization Period ( $T_P$ ) on the Optical Properties of Nanoporous Anodic**  
49  
50 **Alumina Microcavities.** To demonstrate the tuneability of the position of the resonance band  
51  
52 across the spectral regions and to further optimize the quality of NAA- $\mu$ CVs produced by  
53  
54 ASPA, we produced a set of NAA- $\mu$ CVs with different  $T_P$ , where this fabrication parameter  
55  
56  
57  
58  
59  
60

1  
2  
3 was systematically modified from 800 to 1300 s with  $\Delta T_P = 100$  s, while keeping constant  
4  
5  $J_{offset}$  and  $\Delta A_J$  at  $0.280 \text{ mA cm}^{-2}$  and  $0.210 \text{ mA cm}^{-2}$ , respectively. The anodization profiles  
6  
7 and transmission spectra of these NAA- $\mu$ CVs are shown in **Figure S3 (Supporting**  
8  
9 **Information)** and **Figure 9**, respectively. **Figures 9a-d** show the transmission spectra of  
10  
11 these NAA- $\mu$ CVs as a function of  $T_P$  and  $t_{pw}$  (i.e. from 0 to 6 min) and **Figure 10** shows  
12  
13 magnified views of the resonance bands and Gaussian fittings used to estimate  $\lambda_R$ ,  $FWHM_R$   
14  
15 and  $Q_C$ . In all these cases it is verified that the PSB and resonance band of these NAA- $\mu$ CVs  
16  
17 is red-shifted with  $T_P$  and blue shifted with  $t_{pw}$ . Note that those NAA- $\mu$ CVs produced with  
18  
19  $T_P > 800$  s also showed second and third order PSBs. NAA- $\mu$ CVs fabricated with  $T_P = 900$  s  
20  
21 have both first and second order PSBs, while NAA- $\mu$ CVs produced at  $T_P = 1000, 1100, 1200$   
22  
23 and  $1300$  s show second and third order PSBs. However, the first order PSB plays the  
24  
25 primary role in determining the optical properties of NAA- $\mu$ CVs since this band is much  
26  
27 more intense and well-resolved than their higher order counterparts. At  $t_{pw} = 0$  min (**Figure**  
28  
29 **9a**), all NAA- $\mu$ CVs display a weak resonance band within their first order PSB, which is in  
30  
31 the range of 400 to 700 nm and red-shifted with  $T_P$ . As  $T_P$  increases, the intensity of the  
32  
33 resonance band increases and shifts its position ( $\lambda_R$ ) toward the NIR spectral region. As the  
34  
35 digital pictures shown in **Figures 9a-d** (insets) indicate, for a given  $t_{pw}$  the interferometric  
36  
37 color of these NAA- $\mu$ CVs is red-shifted with  $T_P$ . For instance, at  $t_{pw} = 0$  min, the  
38  
39 interferometric color of NAA- $\mu$ CVs changes from transparent (i.e. UV region) ( $T_P = 800$  s),  
40  
41 blue ( $T_P = 900$  s), green ( $T_P = 1000$  s), orange ( $T_P = 1100$  s) to transparent (i.e. NIR region)  
42  
43 ( $T_P = 1200$  and  $1300$  s) as  $T_P$  increases. It is also verified that the resonance band increases its  
44  
45 intensity and it is blue-shifted with a pore widening treatment (i.e.  $t_{pw}$  increases), which is in  
46  
47 good agreement with our previous observation.  
48  
49  
50  
51  
52  
53  
54  
55  
56  
57  
58  
59  
60



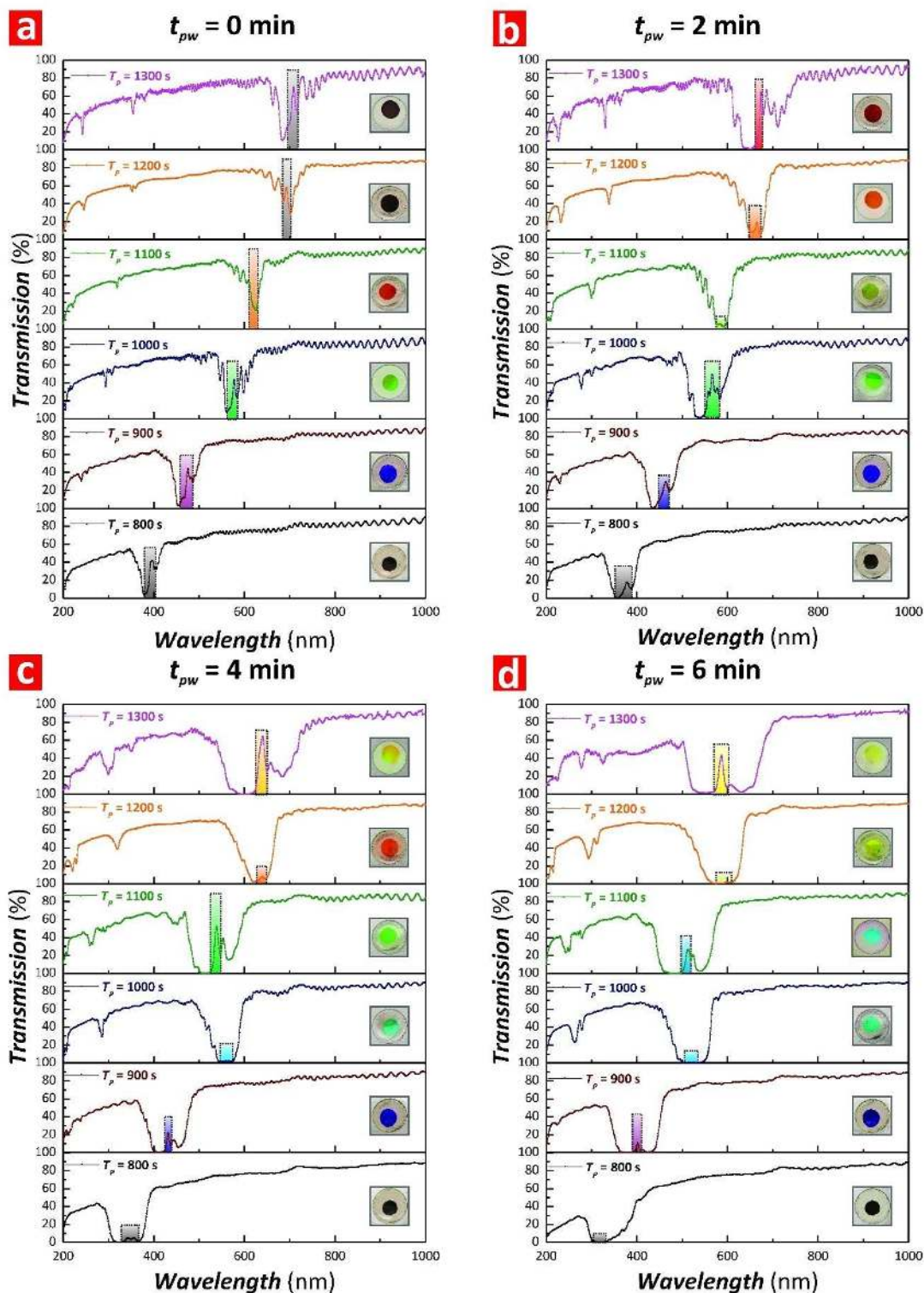


**Figure 9.** Combinational effect of anodization period ( $T_p$ ) and pore widening time ( $t_{pw}$ ) on the optical properties of NAA- $\mu$ CVs (i.e. quality factor –  $Q_C$ , position of resonance band –  $\lambda_R$ , and interferometric color) produced by ASPA. a-d) Transmission spectra showing the position of the resonance band (colored rectangles) and digital pictures (insets) of NAA- $\mu$ CVs for each anodization period ( $T_p = 800$ – $1300$  s) at different pore widening times (i.e. a)  $t_{pw} = 0$  min, b)  $t_{pw} = 2$  min, c)  $t_{pw} = 4$  min, and d)  $t_{pw} = 6$  min).

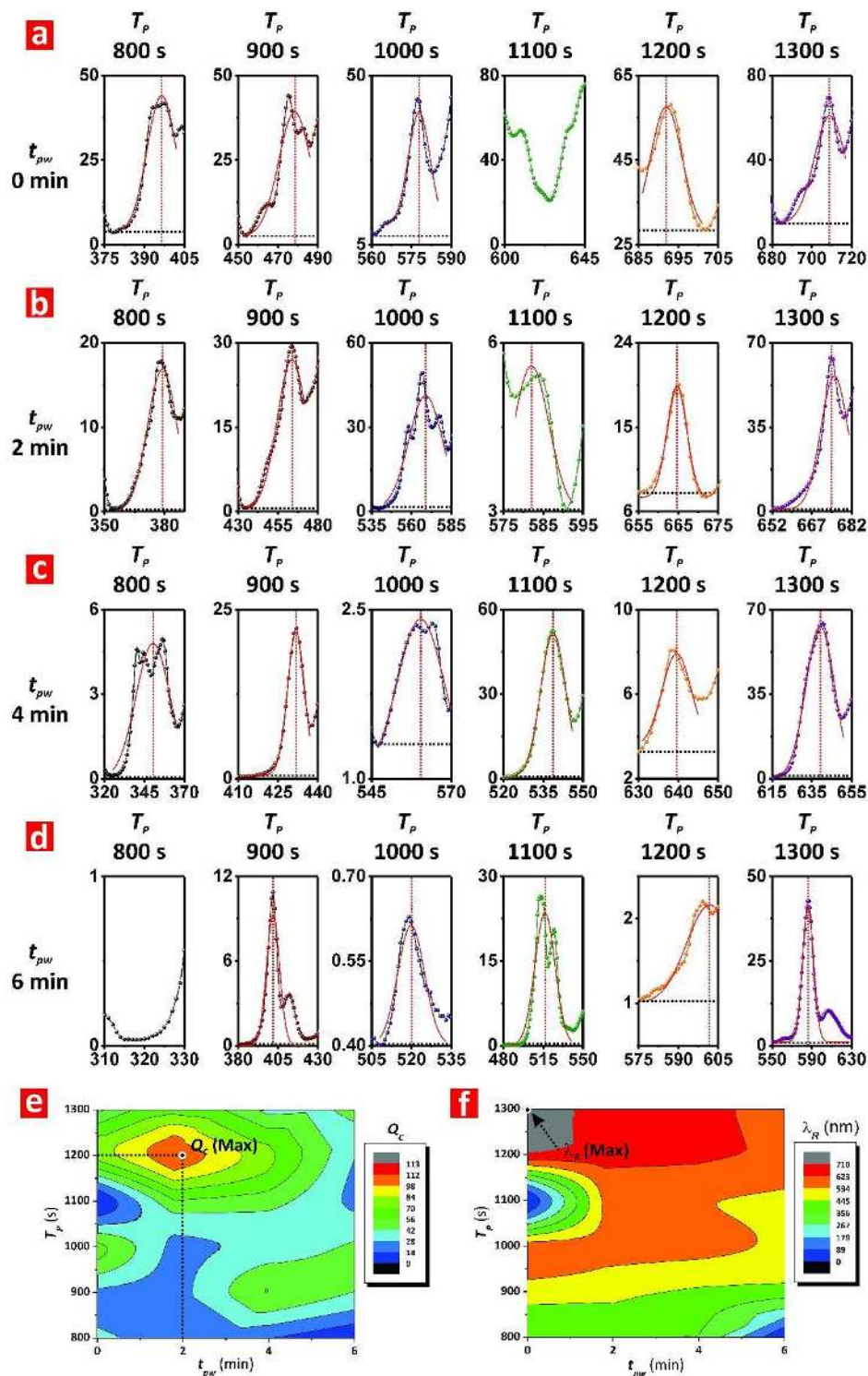


**Figure 10.** Combinational effect of anodization period ( $T_p$ ) and pore widening time ( $t_{pw}$ ) on the resonance band of NAA- $\mu$ CVs produced by ASPA (note: horizontal dotted black lines denote the baseline ( $y_0$ ) used for the Gaussian fittings, which correspond to the lower lobe of the PSB, and vertical dotted red lines indicate the central wavelength of the resonance band ( $\lambda_R$ ) and the symmetry of the Gaussian fitting). a)  $t_{pw} = 0$  min. b)  $t_{pw} = 2$  min. c)  $t_{pw} = 4$  min. d)  $t_{pw} = 6$  min. e) Contour map showing the dependency of  $Q_C$  with  $T_p$  and  $t_{pw}$  for NAA- $\mu$ CVs produced with  $T_p = 800$ – $1300$  s. f) Contour map showing the dependency of  $\lambda_R$  with  $T_p$  and  $t_{pw}$  for NAA- $\mu$ CVs produced with  $T_p = 800$ – $1300$  s.

1  
2  
3 **Figures 10e and f** show contour maps depicting the graphical correlation of  $Q_C$  and  $\lambda_R$  of  
4 NAA- $\mu$ CVs with  $T_P$  and  $t_{pw}$  (**Table S2**). **Figure 10e** reveals that the color fields in the region  
5 of shorter  $T_P$  (i.e. from 800 to 1000 s) are relatively broad across  $t_{pw}$ , from 0 to 6 min, which  
6 is a visual indication of the weak correlation of  $Q_C$  with the fabrication parameters for NAA-  
7  $\mu$ CVs produced at shorter  $T_P$ . Therefore, NAA- $\mu$ CVs produced at  $T_P = 800, 900$  and  $1000$  s  
8 have low  $Q_C$ . In contrast, the color fields become denser with closer field lines when  $T_P$   
9 increases from 1100 to 1300 s. This suggests that  $Q_C$  has a stronger dependency with longer  
10  $T_P$ , where the maximum of  $Q_C$  (i.e.  $112.6 \pm 5.2$ ) is achieved at  $T_P = 1200$  s and  $t_{pw} = 2$  min.  
11 The average  $Q_C$  estimated for NAA- $\mu$ CVs as a function of  $T_P$ , excluding those PCs without  
12 resonance band, was  $44.5 \pm 23.1$ . However, seven of these NAA- $\mu$ CVs showed superior  
13 light-confining performance than those reported in previous studies (i.e.  $Q_C = 56.8 \pm 3.2$  at  $T_P$   
14  $= 900$  s and  $t_{pw} = 4$  min,  $Q_C = 60.2 \pm 2.1$  at  $T_P = 1000$  s and  $t_{pw} = 0$  min,  $Q_C = 56.5 \pm 1.5$  at  
15  $T_P = 1100$  s and  $t_{pw} = 2$  min,  $Q_C = 75.2 \pm 3.3$  at  $T_P = 1200$  s and  $t_{pw} = 0$  min,  $Q_C = 112.6 \pm 5.2$   
16 at  $T_P = 1200$  s and  $t_{pw} = 2$  min,  $Q_C = 73.5 \pm 4.1$  at  $T_P = 1200$  s and  $t_{pw} = 4$  min, and  $Q_C = 63.1$   
17  $\pm 1.2$  at  $T_P = 1300$  s and  $t_{pw} = 2$  min). The distribution of  $\lambda_R$  as a function of  $T_P$  and  $t_{pw}$  is  
18 depicted in **Figure 10f**. This graph shows two local minima in the contour plot due to the  
19 absence of resonance bands within the PSB of these NAA- $\mu$ CVs, which are located at  $t_{pw} = 0$   
20 min for  $T_P = 1100$  s as well as at  $t_{pw} = 6$  min for  $T_P = 800$  s. At  $t_{pw} = 2$  and 4 min, the color  
21 distribution reveals a red shift in  $\lambda_R$  resulting from the manipulation of  $T_P$  from 800 to 1300 s,  
22 where the longest resonance wavelength is achieved at  $T_P = 1300$  s and  $t_{pw} = 0$  min (i.e.  $709 \pm$   
23  $1$  nm). In general, the longer the anodization period, the longer the wavelength at which  
24 NAA- $\mu$ CVs confine light. This analysis also indicates that an increase in  $t_{pw}$  results in a blue  
25 shift of  $\lambda_R$ , thus NAA- $\mu$ CVs confine light of shorter wavelengths although in a less efficient  
26 manner as indicated by the  $Q_C$  analysis shown in **Figure 10e** due to light scattering effect.  
27  
28  
29  
30  
31  
32  
33  
34  
35  
36  
37  
38  
39  
40  
41  
42  
43  
44  
45  
46  
47  
48  
49  
50  
51  
52  
53  
54  
55  
56  
57  
58  
59  
60

### 3.4. Effect of Current Density Offset ( $J_{offset}$ ) on the Optical Properties of Nanoporous

**Anodic Alumina Microcavities.** To further understand the effect of the different fabrication parameters on the photonic features of NAA- $\mu$ CVs produced by ASPA, we investigated the how the current density offset ( $J_{offset}$ ) affects the quality factor and the tuning of resonance bands of NAA- $\mu$ CVs. To this end,  $J_{offset}$  was systematically modified from 0.140 to 0.560 mA cm<sup>-2</sup> with an interval of 0.140 mA cm<sup>-2</sup> while keeping constant the rest of fabrication parameters (i.e.  $T_p = 1300$  s,  $J_{offset} = 0.280$  mA cm<sup>-2</sup>, and  $\Delta A_J = 0.210$  mA cm<sup>-2</sup>). The anodization profiles of NAA- $\mu$ CVs produced at different  $J_{offset}$  are compiled in **Figure S4 (Supporting Information)**. The transmission spectra of these NAA- $\mu$ CVs shown in **Figures 11a-d** were analyzed to establish the effect of this fabrication parameter on  $Q_C$  and  $\lambda_R$ . **Figure 11a** shows the transmission spectra of NAA- $\mu$ CVs produced at  $J_{offset} = 0.140$  mA cm<sup>-2</sup> as a function of  $t_{pw}$  (i.e. 0 to 6 min). The PSB of this set of NAA- $\mu$ CVs is located within the visible region, with a very weak resonance band that is almost vanished at long pore widening times (i.e.  $t_{pw} > 2$  min). The pore widening treatment blue-shifts the position of the PSB and leads the NAA- $\mu$ CV to lose its light-confining characteristics. The transmission spectra shown in **Figure 11b** reveals that the position of the PSB of NAA- $\mu$ CVs produced at  $J_{offset} = 0.280$  mA cm<sup>-2</sup> are located within the upper range of visible spectrum (i.e. 600–800 nm). Unlike NAA- $\mu$ CVs produced at  $J_{offset} = 0.140$  mA cm<sup>-2</sup>, the resonance band of these NAA- $\mu$ CVs ( $J_{offset} = 0.280$  mA cm<sup>-2</sup>) remains well-resolved and sharp after pore widening from 0 to 6 min. On the other hand, both sets of NAA- $\mu$ CVs produced at  $J_{offset} = 0.420$  and 0.560 mA cm<sup>-2</sup> have their PSBs located in the NIR range (i.e. 900–1100 nm) (**Figures 11c and d**). These NAA- $\mu$ CVs also show the presence of an intense resonance band within their PSB, which is slightly widen and blue-shifted with the pore widening treatment, from 0 to 6 min.



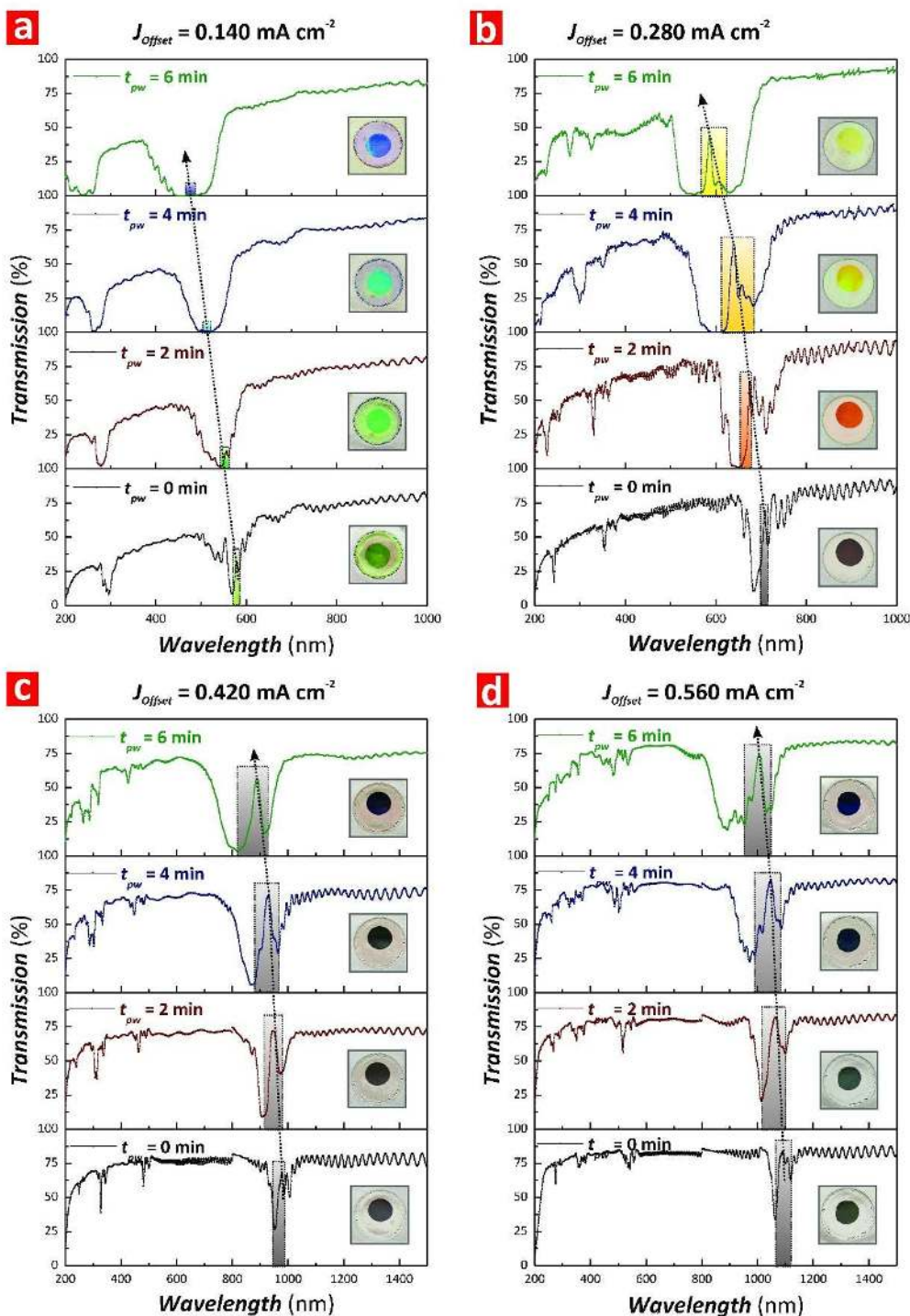


**Figure 11.** Combinational effect of anodization offset ( $J_{\text{Offset}}$ ) and pore widening time ( $t_{pw}$ ) on the optical properties of NAA- $\mu$ CVs (i.e. quality factor –  $Q_C$ , position of resonance band –  $\lambda_R$ , and interferometric color) produced by ASPA. a-d) Transmission spectra showing the position of the resonance band, digital pictures (insets) of NAA- $\mu$ CVs for each anodization offset ( $J_{\text{Offset}} = 0.140$ – $0.560 \text{ mA cm}^{-2}$ ) at different pore widening times (from 0 to 6 min) (i.e. a)  $J_{\text{Offset}} = 0.140 \text{ mA cm}^{-2}$ , b)  $J_{\text{Offset}} = 0.280 \text{ mA cm}^{-2}$ , c)  $J_{\text{Offset}} = 0.420 \text{ mA cm}^{-2}$ , and d)  $J_{\text{Offset}} = 0.560 \text{ mA cm}^{-2}$ ) (note: color rectangles denote the approximate position of the resonance band within the PSB and black dotted arrow lines indicate the blue shift of the resonance bands with  $t_{pw}$ ).

1  
2  
3 By comparing the transmission spectra at different  $J_{offset}$ , it is apparent that an increase in  
4  
5  $J_{offset}$  causes a red shift in the position of resonance band. As the digital images shown in the  
6  
7 insets in **Figures 11a-d** demonstrate, these NAA- $\mu$ CVs display vivid interferometric colors,  
8  
9 which are affected by the fabrication parameters:  $J_{offset}$  and  $t_{pw}$ . Although these NAA- $\mu$ CVs  
10  
11 show second and third order PSBs, the color displayed by these PCs corresponds to the  
12  
13 wavelength at which the first order PSB is located, denoting a more efficient reflection of  
14  
15 light within these spectral regions. In this case, NAA- $\mu$ CVs produced at lower  $J_{offset}$  (i.e.  
16  
17 0.140 and 0.280 mA cm<sup>-2</sup>) display vivid colors corresponding to the position of their PSB in  
18  
19 the visible spectral range. In contrast, the PSBs of NAA- $\mu$ CVs produced with high  $J_{offset}$  (i.e.  
20  
21 0.420 and 0.560 mA cm<sup>-2</sup>) are within the NIR range, thus no color is observed (i.e.  
22  
23 transparent – black). **Figures 12a-d** show magnified views of the resonance bands and  
24  
25 Gaussian fittings used to estimate  $\lambda_R$ ,  $FWHM_R$  and  $Q_C$  for these NAA- $\mu$ CVs and **Figures 12e**  
26  
27 **and f** compile a summary of the estimated values for  $Q_C$  and  $\lambda_R$  in the form of contour maps.  
28  
29 The visual analysis of the magnified resonance bands shown in **Figures 12a-d** reveals that, in  
30  
31 general, the intensity of the resonance band increases with  $J_{offset}$  and decreases with  $t_{pw}$ . A  
32  
33 closer analysis of the values of  $Q_C$ , visually shown in **Figure 12e** and compiled in **Table S3**  
34  
35 **(Supporting Information)**, reveals that the combination of low values of  $J_{offset}$  (e.g. 0.140-  
36  
37 0.280 mA cm<sup>-2</sup>) and moderate pore widening times (i.e. 2-4 min) are favorable in the  
38  
39 production of NAA- $\mu$ CVs with high quality resonance bands. The  $Q_C$  maximum is achieved  
40  
41 by NAA- $\mu$ CVs produced with  $J_{offset} = 0.140$  mA cm<sup>-2</sup> and  $t_{pw} = 4$  min (i.e.  $65.5 \pm 2.3$ ),  
42  
43 although these PC structure show considerably weaker resonance bands as compared to their  
44  
45 counterparts produced at higher  $J_{offset}$  (i.e.  $> 0.140$  mA cm<sup>-2</sup>). The dependency of  $Q_C$  on  $J_{offset}$   
46  
47 increases within the range 0.140-0.420 mA cm<sup>-2</sup>, as denoted by the denser color fields with  
48  
49 short distance between adjacent field lines.  
50  
51  
52  
53  
54  
55  
56  
57  
58  
59  
60

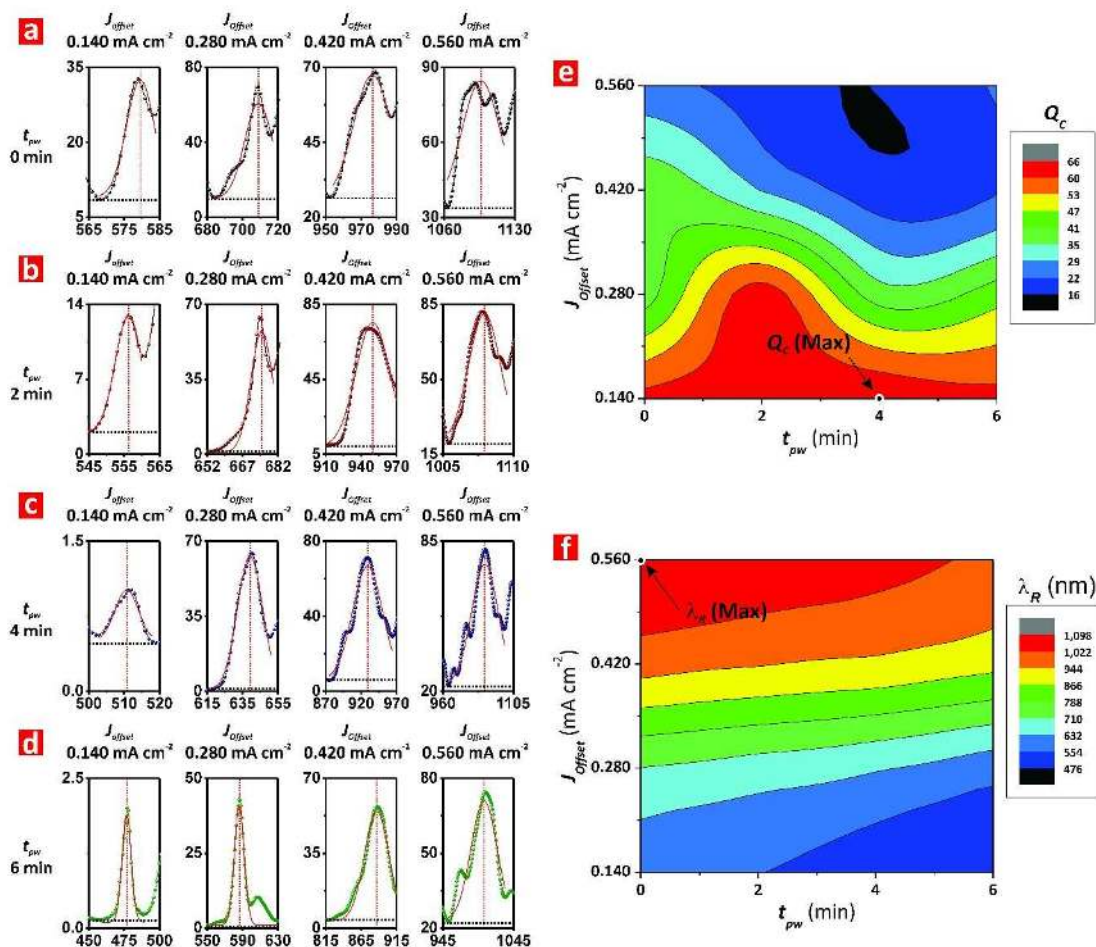


**Figure 12.** Combinational effect of current density offset ( $J_{Offset}$ ) and pore widening time ( $t_{pw}$ ) on the resonance band of NAA- $\mu$ CVs produced by ASPA (note: horizontal dotted black lines denote the baseline ( $\nu_0$ ) used for the Gaussian fittings, which correspond to the lower lobe of the PSB, and vertical dotted red lines indicate the central wavelength of the resonance band ( $\lambda_R$ ) and the symmetry of the Gaussian fitting). a)  $J_{Offset} = 0.140 \text{ mA cm}^{-2}$ , b)  $J_{Offset} = 0.280 \text{ mA cm}^{-2}$ , c)  $J_{Offset} = 0.420 \text{ mA cm}^{-2}$ , and d)  $J_{Offset} = 0.560 \text{ mA cm}^{-2}$ . e) Contour map showing the dependency of  $Q_C$  with  $J_{Offset}$  and  $t_{pw}$  for NAA- $\mu$ CVs produced with  $J_{Offset} = 0.140\text{--}0.560 \text{ mA cm}^{-2}$ . f) Contour map showing the dependency of  $\lambda_R$  with  $J_{Offset}$  and  $t_{pw}$  for NAA- $\mu$ CVs produced with  $J_{Offset} = 0.140\text{--}0.560 \text{ mA cm}^{-2}$ .

The broad color fields and more separated field lines at the region of high  $J_{Offset}$  and long  $t_{pw}$  suggest a weak dependency of  $Q_C$  with these combinations of fabrication parameters, which worsens the quality of the microcavity structure. The average  $Q_C$  estimated for NAA- $\mu$ CVs as a function of  $J_{Offset}$  was  $39.1 \pm 18.4$  and five of these NAA- $\mu$ CVs showed slightly superior light-confining performance than those reported in previous studies (i.e.  $Q_C = 61.7 \pm 2.2$  at  $J_{Offset} = 0.140 \text{ mA cm}^{-2}$  and  $t_{pw} = 0 \text{ min}$ ,  $Q_C = 62.5 \pm 3.4$  at  $J_{Offset} = 0.140 \text{ mA cm}^{-2}$  and  $t_{pw} = 2 \text{ min}$ ,  $Q_C = 65.5 \pm 3.6$  at  $J_{Offset} = 0.140 \text{ mA cm}^{-2}$  and  $t_{pw} = 4 \text{ min}$ ,  $Q_C = 61.9 \pm 2.4$  at  $J_{Offset} =$

1  
2  
3 0.140 mA cm<sup>-2</sup> and  $t_{pw} = 6$  min, and  $Q_C = 63.1 \pm 1.2$  at  $J_{offset} = 0.280$  mA cm<sup>-2</sup> and  $t_{pw} = 2$   
4  
5 min). The effect of  $J_{offset}$  and  $t_{pw}$  on the position of the resonance band of NAA- $\mu$ CVs is  
6  
7 summarized in the contour map shown in **Figure 12f**. This contour map shows that the field  
8  
9 line distances at low  $J_{offset}$  (i.e.  $J_{offset} < 0.280$  mA cm<sup>-2</sup>) and high  $J_{offset}$  (i.e.  $J_{offset} > 0.420$  mA  
10  
11 cm<sup>-2</sup>) are relatively wide. However, the color fields become closer with shorter equidistant  
12  
13 field lines for  $J_{offset}$  between 0.280 and 0.420 mA cm<sup>-2</sup>, which indicates a stronger dependency  
14  
15 of  $\lambda_R$  with  $J_{offset}$  within that range of fabrication parameters. It is verified that  $\lambda_R$  is red-shifted  
16  
17 towards the NIR region by increasing  $J_{offset}$ . The higher  $J_{offset}$  is, the longer the wavelength at  
18  
19 which light is confined within the structure of NAA- $\mu$ CVs produced by ASPA. The  
20  
21 maximum value of  $\lambda_R$  (i.e.  $1096 \pm 1$  nm) is located at  $J_{offset} = 0.560$  mA cm<sup>-2</sup> and  $t_{pw} = 0$  min.  
22  
23 An increase in  $t_{pw}$  has an opposite effect to that of  $J_{offset}$  on the shifting of  $\lambda_R$ . However,  $J_{offset}$   
24  
25 has a more significant effect on the position of the resonance band as denoted by the color  
26  
27 field distribution.  
28  
29  
30

## 31 32 CONCLUSIONS

33  
34 In summary, this study has demonstrated that a rational design of the nanoporous  
35  
36 structure of NAA-based optical microcavities using apodized stepwise pulse anodization can  
37  
38 lead to an enhancement of the light-confining capabilities of these PCs. The structure of these  
39  
40 optical microcavities is composed of two apodized NAA-DBRs, which can confine light  
41  
42 efficiently (i.e.  $Q_C = 112.6 \pm 5.2$ ). Furthermore, this nanofabrication approach enables the  
43  
44 fine-tuning of the optical properties of the two highly reflective mirrors so light can be  
45  
46 confined within the PC structure more efficiently across the spectral regions. The optical  
47  
48 properties of NAA-based optical microcavities were assessed in terms of quality factor,  
49  
50 position of resonance band, and interferometric colors. The anodization parameters  
51  
52 investigated were anodization period, anodization time, current density offset and pore  
53  
54  
55  
56  
57  
58  
59  
60



1  
2  
3 widening time. A systematic modification of these parameters allowed to establish  
4  
5 optimization paths toward more efficient light-confining NAA-based PC structures.  
6

7 In general, our study established that a combination of longer anodization time, longer  
8  
9 anodization period, short pore widening time, and moderate current density offset generates  
10  
11 optical microcavities with high quality factor, where the most optimal NAA- $\mu$ CV was that  
12  
13 produced with 20 h anodization time, 1200 s anodization period, 2 min of pore widening, and  
14  
15 0.280 mA cm<sup>-2</sup> of current density offset. Our results provide a better understanding and solid  
16  
17 foundation to further enhance the light-confining capabilities of NAA-based optical  
18  
19 microcavities, opening new opportunities for further fundamental and applied research for  
20  
21 these nanoporous PC structures in optical sensing, photonics, and optoelectronics.  
22  
23  
24

## 25 **Supporting Information**

26  
27 The Supporting Information file provides information about the structure of NAA- $\mu$ CVs at  
28  
29 different pore widening times, anodization profiles of NAA- $\mu$ CVs produced by ASPA at  
30  
31 different anodization periods, from 800 to 1300 s, and current density offsets, from 0.140 to  
32  
33 0.560 mA cm<sup>-2</sup>, and a compilation of the values of  $y_0$ ,  $\lambda_R$ ,  $FWHM_R$ ,  $Q_C$ , and  $R^2$ .  
34  
35  
36

## 37 **Author Information**

### 38 Doctor Abel Santos

39 Research for Impact Fellow – Lecturer

40 School of Chemical Engineering – The University of Adelaide

41 Phone: +61 8 8313 1535

42 Email: [abel.santos@adelaide.edu.au](mailto:abel.santos@adelaide.edu.au)

43 Web page: <http://www.adelaide.edu.au/directory/abel.santos>

### 44 Professor Andrew Abell

45 Professor of Chemistry and node director of the ARC Centre of Excellence for Nanoscale  
46  
47 Biophotonics

48 School of Chemistry and Physics – The University of Adelaide

49 Phone: + 61 8 8313 5652  
50  
51  
52  
53  
54  
55  
56  
57  
58  
59  
60

Email: [andrew.abell@adelaide.edu.au](mailto:andrew.abell@adelaide.edu.au)

Web page: <http://researchers.adelaide.edu.au/profile/andrew.abell#contact-details>

### Acknowledgements

Authors thank the support provided by the Australian Research Council (ARC) through the grants number DE140100549 and CE140100003, the School of Chemical Engineering, the University of Adelaide (DVCR initiative 'Research for Impact'), the Institute for Photonics and Advanced Sensing (IPAS), and the ARC Centre of Excellence for Nanoscale BioPhotonics (CNBP).

### REFERENCES

- 1 Michler, P.; Kiraz, A.; Becher, C.; Schoenfeld, W.; Petroff, P.; Zhang, L.; Hu, E.; Imamoglu, A. A quantum dot single-photon turnstile device. *Science* **2000**, *290*, 2282-2285.
- 2 Ogawa, S.; Imada, M.; Yoshimoto, S.; Okano, M.; Noda, S. Control of light emission by 3D photonic crystals. *Science* **2004**, *305*, 227-229.
- 3 Noda, S.; Chutinan, A.; Imada, M. Trapping and emission of photons by a single defect in a photonic bandgap structure. *Nature* **2000**, *407*, 608-610.
- 4 Song, B.-S.; Asano, T.; Noda, S. Physical origin of the small modal volume of ultra-high-Q photonic double-heterostructure nanocavities. *New J. Phys.* **2006**, *8*, 209.
- 5 Notomi, M. Manipulating light with strongly modulated photonic crystals. *Rep. Prog. Phys.* **2010**, *73*, 096501.
- 6 Lee, H.; Chen, T.; Li, J.; Yang, K.Y.; Jeon, S.; Painter, O.; Vahala, K.J. Chemically etched ultrahigh-Q wedge-resonator on a silicon chip. *Nat. Photonics* **2012**, *6*, 369-373.
- 7 Vahala, K.J. Optical microcavities. *Nature* **2003**, *424*, 839-846.
- 8 Matsko, A. B. *Practical applications of microresonators in optics and photonics*. Boca Raton: CRC Press, 2009.

- 1  
2  
3 9 Yablonovitch, E. Inhibited spontaneous emission in solid-state physics and electronics.  
4 *Phys. Rev. Lett.* **1987**, *58*, 2059.  
5  
6  
7 10 John, S. Strong localization of photons in certain disordered dielectric superlattices. *Phys.*  
8 *Rev. Lett.*, 1987, **58**, 2486.  
9  
10  
11 11 Krauss, T.F. Photonic crystals: Cavities without leaks. *Nature Mater.* **2003**, *2*, 777-778.  
12  
13 12 Foresi, J.; Villeneuve, P.R.; Ferrera, J.; Thoen, E.; Steinmeyer, G.; Fan, S.; Joannopoulos,  
14 J.; Kimerling, L.; Smith, H. I.; Ippen, E. Photonic-bandgap microcavities in optical  
15 waveguides. *Nature* **1997**, *390*, 143-145.  
16  
17  
18 13 Sun, H.-B.; Mizeikis, V.; Xu, Y.; Juodkazis, S.; Ye, J.-Y.; Matsuo, S.; Misawa, H.  
19 Microcavities in polymeric photonic crystals. *Appl. Phys. Lett.* **2001**, *79*, 1-3.  
20  
21  
22 14 Ripin, D.J.; Lim, K.-Y.; Petrich, G.; Villeneuve, P.R.; Fan, S.; Thoen, E.; Joannopoulos, J.  
23 D.; Ippen, E.; Kolodziejcki, L. One-dimensional photonic bandgap microcavities for  
24 strong optical confinement in GaAs and GaAs/AlxOy semiconductor waveguides. *J.*  
25 *Lightwave Technol.* **1999**, *17*, 2152.  
26  
27  
28 15 Baba, T. Photonic crystals and microdisk cavities based on GaInAsP-InP system. *IEEE J.*  
29 *Sel. Top. Quantum Electron.* **1997**, *3*, 808-830.  
30  
31  
32 16 Solomon, G.; Pelton, M.; Yamamoto, Y. Single-mode spontaneous emission from a  
33 single quantum dot in a three-dimensional microcavity. *Phys. Rev. Lett.* **2001**, *86*, 3903.  
34  
35  
36 17 Benson, T.M.; Boriskina, S.V.; Sewell, P.; Vukovic, A.; Greedy, S.C.; Nosich, A.I.  
37 Micro-optical resonators for microlasers and integrated optoelectronics. In *Frontiers in*  
38 *planar lightwave circuit technology*, Springer: 2006; pp 39-70.  
39  
40  
41 18 Zain, A.R.M.; Johnson, N.P.; Sorel, M.; Richard, M. Ultra high quality factor one  
42 dimensional photonic crystal/photonic wire micro-cavities in silicon-on-insulator (SOI).  
43 *Opt. Express* **2008**, *16*, 12084-12089.  
44  
45  
46 19 Akahane, Y.; Asano, T.; Song, B.-S.; Noda, S. High-Q photonic nanocavity in a two-  
47 dimensional photonic crystal. *Nature* **2003**, *425*, 944-947.  
48  
49  
50 20 Pavesi, L.; Mazzoleni, C.; Tredicucci, A.; Pellegrini, V. Controlled photon emission in  
51 porous silicon microcavities. *Appl. Phys. Lett.* **1995**, *67*, 3280-3282.  
52  
53  
54  
55  
56  
57  
58  
59  
60

- 1  
2  
3 21 Pellegrini, V.; Tredicucci, A.; Mazzoleni, C.; Pavesi, L. Enhanced optical properties in  
4 porous silicon microcavities. *Phys. Rev. B* **1995**, *52*, R14328.  
5  
6  
7 22 Cazzanelli, M.; Pavesi, L. Time-resolved photoluminescence of all-porous-silicon  
8 microcavities. *Phys. Rev. B* **1997**, *56*, 15264.  
9  
10  
11 23 Ghulinyan, M.; Oton, C.; Bonetti, G.; Gaburro, Z.; Pavesi, L. Free-standing porous silicon  
12 single and multiple optical cavities. *J. Appl. Phys.* **2003**, *93*, 9724-9729.  
13  
14  
15 24 Pavesi, L.; Panzarini, G.; Andreani, L. All-porous silicon-coupled microcavities:  
16 Experiment versus theory. *Phys. Rev. B* **1998**, *58*, 15794.  
17  
18  
19 25 De Stefano, L.; Moretti, L.; Rendina, I.; Rossi, A. M. Porous silicon microcavities for  
20 optical hydrocarbons detection. *Sens. Actuators, A* **2003**, *104*, 179-182.  
21  
22  
23 26 Mulloni, V.; Pavesi, L. Porous silicon microcavities as optical chemical sensors. *Appl.*  
24 *Phys. Lett.* **2000**, *76*, 2523-2525.  
25  
26  
27 27 Reece, P.; Léron del, G.; Zheng, W.; Gal, M. Optical microcavities with subnanometer  
28 linewidths based on porous silicon. *Appl. Phys. Lett.* **2002**, *81*, 4895-4897.  
29  
30  
31 28 Lehmann, V. *Electrochemistry of Silicon: Instrumentation, Science, Materials and*  
32 *Applications*. Wiley: 2002.  
33  
34  
35 29 Chen, Y.; Santos, A.; Wang, Y.; Kumeria, T.; Li, J.; Wang, C.; Losic, D. Biomimetic  
36 nanoporous anodic alumina distributed bragg reflectors in the form of films and  
37 microsized particles for sensing applications. *ACS Appl. Mater. Interfaces* **2015**, *7*,  
38 19816-19824.  
39  
40  
41  
42 30 Yu, M.; Li, C.; Yang, Y.; Xu, S.; Zhang, K.; Cui, H.; Zhu, X. Cavities between the double  
43 walls of nanotubes: Evidence of oxygen evolution beneath an anion-contaminated layer.  
44 *Electrochem. Commun.* **2018**, *90*, 34-38.  
45  
46  
47  
48 31 Yu, M.; Chen, Y.; Li, C.; Yan, S.; Cui, H.; Zhu, X.; Kong, J. Studies of oxide growth  
49 location on anodization of Al and Ti provide evidence against the field-assisted  
50 dissolution and field-assisted ejection theories. *Electrochem. Commun.* **2018**, *87*, 76-80.  
51  
52  
53  
54 32 Yu, M.; Cui, H.; Ai, F.; Jiang, L.; Kong, J.; Zhu, X. Terminated nanotubes: Evidence  
55 against the dissolution equilibrium theory. *Electrochem. Commun.* **2018**, *86*, 80-84.  
56  
57  
58  
59  
60

- 1  
2  
3 33 Zhao, S.; Xing, J.; Fan, H.; Zhang, S.; Li, D.; Zhu, X. Derivation of a mathematical model  
4 for the growth of anodic TiO<sub>2</sub> nanotubes under constant current conditions. *J.*  
5 *Electrochem. Soc.* **2017**, *164*, E187-E193.  
6  
7  
8  
9 34 Wen, L.; Xu, R.; Mi, Y.; Lei, Y. Multiple nanostructures based on anodized aluminium  
10 oxide templates. *Nat. Nanotechnol.* **2017**, *12*, 244-250.  
11  
12  
13 35 Xu, R.; Wen, L.; Wang, Z.; Zhao, H.; Xu, S.; Mi, Y.; Xu, Y.; Sommerfeld, M.; Fang, Y.;  
14 Lei, Y. Three-dimensional plasmonic nanostructures design for boosting  
15 photoelectrochemical activity. *ACS Nano* **2017**, *11*, 7382-7389.  
16  
17  
18 36 Zhan, Z.; Xu, R.; Mi, Y.; Zhao, H.; Lei, Y. Highly controllable surface plasmon  
19 resonance property by heights of ordered nanoparticle arrays fabricated via a  
20 nonlithographic route. *ACS Nano* **2015**, *9*, 4583-4590.  
21  
22  
23  
24 37 Lee, J.; Bae, K.; Kang, G.; Choi, M.; Baek, S.; Yoo, D.-S.; Lee, C.-W.; Kim, K. Graded-  
25 lattice AAO photonic crystal heterostructure for high *Q* refractive index sensing. *RSC Adv.*  
26 **2015**, *5*, 71770-71777.  
27  
28  
29  
30 38 Wang, Y.; Chen, Y.; Kumeria, T.; Ding, F.; Evdokiou, A.; Losic, D.; Santos, A. Facile  
31 synthesis of optical microcavities by a rationally designed anodization approach: tailoring  
32 photonic signals by nanopore structure. *ACS Appl. Mater. Interfaces* **2015**, *7*, 9879-9888.  
33  
34  
35 39 Shang, G. L.; Fei, G. T.; De Zhang, L. Experimental realization of tunable defect mode in  
36 photonic crystal. *J. Phys. D: Appl. Phys.* **2015**, *48*, 435304.  
37  
38  
39 40 Lee, W.; Schwirn, K.; Steinhart, M.; Pippel, E.; Scholz, R.; Gösele, U. Structural  
40 engineering of nanoporous anodic aluminium oxide by pulse anodization of aluminium.  
41 *Nat. Nanotechnol.* **2008**, *3*, 234-239.  
42  
43  
44  
45 41 Yan, P.; Fei, G.-T.; Li, H.; Shang, G.-L.; Wu, B.; Zhang, L.-D. Alumina photonic crystals  
46 with defect modes for sensor application. *Chin. J. Chem. Phys.* 2014, *27*, 121-124.  
47  
48  
49 42 Ghulinyan, M.; Oton, C.J.; Bonetti, G.; Gaburro, Z.; Pavesi, L. Free-standing porous  
50 silicon single and multiple optical cavities. *J. Appl. Phys.*, **2003**, *93*, 9724-9729.  
51  
52  
53 43 Reece, P.J.; Léron del, G.; Zheng, W.H.; Gal, M. Optical microcavities with subnanometer  
54 linewidths based on porous silicon. *Appl. Phys. Lett.*, **2002**, *81*, 4895-4897.  
55  
56  
57  
58  
59  
60

- 1  
2  
3 44 Lee, W.; Scholz, R.; Gösele, U. A continuous process for structurally well-defined Al<sub>2</sub>O<sub>3</sub>  
4 nanotubes based on pulse anodization of aluminum. *Nano Lett.* **2008**, *8*, 2155-2160.  
5  
6  
7 45 Lee, W.; Kim, J.-C. Highly ordered porous alumina with tailor-made pore structures  
8 fabricated by pulse anodization. *Nanotechnology* **2010**, *21*, 485304.  
9  
10  
11 46 Lee, W.; Ji, R.; Gösele, U.; Nielsch, K. Fast fabrication of long-range ordered porous  
12 alumina membranes by hard anodization. *Nature Mater.* **2006**, *5*, 741-747.  
13  
14  
15 47 Santos, A. Nanoporous anodic alumina photonic crystals: Fundamentals, developments  
16 and perspectives. *J. Mater. Chem. C* **2017**, *5*, 5581-5599  
17  
18  
19 48 Chen, Y.; Santos, A.; Ho, D.; Wang, Y.; Kumeria, T.; Li, J.; Wang, C.; Losic, D. On the  
20 generation of interferometric colors in high purity and technical grade aluminum: An  
21 alternative green process for metal finishing industry. *Electrochim. Acta* **2015**, *174*, 672-  
22 681.  
23  
24  
25  
26 49 Macias, G.; Ferré-Borrull, J.; Pallarès, J.; Marsal, L.F. 1-D nanoporous anodic alumina  
27 rugate filters by means of small current variations for real-time sensing applications.  
28 *Nanoscale Res. Lett.* **2014**, *9*, 315.  
29  
30  
31  
32 50 Zheng, W.J.; Fei, G.T.; Wang, B.; Jin, Z.; Zhang, L.D. Distributed Bragg reflector made  
33 of anodic alumina membrane. *Mater. Lett.* **2009**, *63*, 706-708.  
34  
35  
36 51 Shang, G.L.; Fei, G.T.; Zhang, Y.; Yan, P.; Xu, S.H.; Zhang, L.D. Preparation of narrow  
37 photonic bandgaps located in the near infrared region and their applications in ethanol gas  
38 sensing. *J. Mater. Chem. C* **2013**, *1*, 5285-5291.  
39  
40  
41  
42 52 Law, C.S.; Santos, A.; Nemati, M.; Losic, D. Structural engineering of nanoporous anodic  
43 alumina photonic crystals by sawtooth-like pulse anodization. *ACS Appl. Mater.*  
44 *Interfaces* **2016**, *8*, 13542-13554.  
45  
46  
47 53 Nemati, M.; Santos, A.; Law, C. S.; Losic, D. Assessment of binding affinity between  
48 drugs and human serum albumin using nanoporous anodic alumina photonic crystals.  
49 *Anal. Chem.* **2016**, *88*, 5971-5980.  
50  
51  
52  
53 54 Santos, A.; Law, C.S.; Lei, D.W.C.; Pereira, T.; Losic, D. Fine tuning of optical signals in  
54 nanoporous anodic alumina photonic crystals by apodized sinusoidal pulse anodisation.  
55 *Nanoscale* **2016**, *8*, 18360-18375.  
56  
57  
58  
59  
60

- 1  
2  
3 55 Santos, A.; Pereira, T.; Law, C.S.; Losic, D. Rational engineering of nanoporous anodic  
4 alumina optical bandpass filters. *Nanoscale* **2016**, *8*, 14846-14857.  
5  
6  
7 56 Santos, A.; Law, C.S.; Pereira, T.; Losic, D. Nanoporous hard data: optical encoding of  
8 information within nanoporous anodic alumina photonic crystals. *Nanoscale* **2016**, *8*,  
9 8091-8100.  
10  
11  
12 57 Nemati, M.; Santos, A.; Kumeria, T.; Losic, D. Label-free real-time quantification of  
13 enzyme levels by interferometric spectroscopy combined with gelatin-modified  
14 nanoporous anodic alumina photonic films. *Anal. Chem.* **2015**, *87*, 9016-9024.  
15  
16  
17  
18 58 Chen, Y.; Santos, A.; Wang, Y.; Kumeria, T.; Ho, D.; Li, J.; Wang, C.; Losic, D. Rational  
19 design of photonic dust from nanoporous anodic alumina films: a versatile photonic  
20 nanotool for visual sensing. *Sci. Rep.* **2015**, *5*, 12893.  
21  
22  
23  
24 59 Kumeria, T.; Rahman, M.M.; Santos, A.; Ferré-Borrull, J.; Marsal, L.F.; Losic, D.  
25 Nanoporous anodic alumina rugate filters for sensing of ionic mercury: Toward  
26 environmental point-of-analysis systems. *ACS Appl. Mater. Interfaces* **2014**, *6*, 12971-  
27 12978.  
28  
29  
30  
31 60 Law, C. S.; Lim, S. Y.; Santos, A. On the precise tuning of optical filtering features in  
32 nanoporous anodic alumina distributed Bragg reflectors. *Sci. Rep.* **2018**, *8*, 4642.  
33  
34  
35 61 Southwell, W. H. Using apodization functions to reduce sidelobes in rugate filters. *Appl.*  
36 *Opt.* **1989**, *28*, 5091-5094.  
37  
38  
39 62 Asano, T.; Song, B.-S.; Noda, S. Analysis of the experimental Q factors (~ 1 million) of  
40 photonic crystal nanocavities. *Opt. Express* **2006**, *14*, 1996-2002.  
41  
42  
43 63 Abràmoff, M.D.; Magalhaes, P.J.; Ram, S.J. Image processing with ImageJ. *Biophotonics*  
44 *Int.*, **2004**, *11*, 36-42.  
45  
46  
47 64 Jalkanen, T.; Mäkilä, E.; Suzuki, Y. I.; Urata, T.; Fukami, K.; Sakka, T.; Salonen, J.;  
48 Ogata, Y. Studies on chemical modification of porous silicon-based graded-index optical  
49 microcavities for improved stability under alkaline conditions. *Adv. Funct. Mater.* **2012**,  
50 *22*, 3890-3898.  
51  
52  
53  
54  
55  
56  
57  
58  
59  
60

1  
2  
3 65 Jenie, S.A.; Pace, S.; Sciacca, B.; Brooks, R.D.; Plush, S.E.; Voelcker, N.H. Lanthanide  
4 luminescence enhancements in porous silicon resonant microcavities. *ACS Appl. Mater.*  
5 *Interfaces* **2014**, *6*, 12012-12021.  
6  
7  
8  
9  
10

## 11 TABLE OF CONTENTS

